

Shock Tube Experimentation Utilizing Advance Diagnostics for the
Study of an Impulsively Accelerated Multiphase Cylinder

A Thesis
presented to
the Faculty of the Graduate School
at the University of Missouri-Columbia

In Partial Fulfillment
of the Requirements for the Degree
Master of Science

by
John B. Middlebrooks
Dr. Jacob A. McFarland, Thesis Supervisor

MAY 2019

The undersigned, appointed by the dean of the Graduate School, have examined the thesis entitled:

Shock Tube Experimentation Utilizing Advance
Diagnostics for the Study of an Impulsively Accelerated
Multiphase Cylinder

presented by John Benjamin Middlebrooks,

a candidate for the degree of Master of Science,

and hereby certify that, in their opinion, it is worthy of acceptance.

Professor Jacob A. McFarland

Professor Frank Feng

Professor Binbin Wang

Acknowledgements

My journey towards this degree has been a rewarding one filled with a multitude of accomplishments and valuable lessons. My success in this endeavor would not have been possible without the support, guidance, and love of others. Many acknowledgements are in order. I must first thank my Mother and Father who have shown me nothing but unconditional love and support throughout my studies. My girlfriend Andrea Riley who makes my life better just by being in it, and all of my family and close friends who have supported me.

I would like to thank the numerous lab mates I have had throughout my studies. I am privileged to call them my colleagues and friends. In particular, Wolfgang Black for his guidance and friendship through my undergraduate and graduate career at the University of Missouri. My friend and lab mate Roy Allen who has taught me about craftsmanship, and the pride in a job well done. Jeevhan Dahal, Manoj Paudel, and Shair Almuhna for showing me the theory and beauty behind computational fluid dynamics. Constantine Avgoustopoulos and Raj Kothakapa for their guidance and efforts in laying the ground work necessary for the experiments I have conducted. Curtis Maxon, who I have had the pleasure of working with closely on both class and research related projects. The undergraduates Calvin Young, Ben Musick, and Nathan Crum for all of their help along the way. My friend and successor Vasco Duke for all of his help in experiments, I know the shock tube will be in good hands.

Lastly I must thank my advisor and mentor, Professor Jacob McFarland. He has supported me when I doubted myself, instructed me whenever needed, and encouraged me to pursue my aspirations as a scientist with vigor. He has nurtured my interest in thermal fluid sciences into a passion, and introduced me to a vibrant community of like-minded scientist. He has truly changed my life for the better, and I am forever grateful. I could not have asked for a better advisor.

TABLE OF CONTENTS

ACKNOWLEDGEMENTS	ii
LIST OF FIGURES	v
ABSTRACT	vii
Chapter	
1. INTRODUCTION AND BACKGROUND.....	1
1.1 Applications.....	1
1.2 Theory: The Richtmyer-Meshkov Instability.....	1
1.3 Theory: The Shock-Driven Multiphase Instability.....	5
1.4 Droplet Effects.....	10
1.5 Previous and Related Works.....	11
2. EXPERIMENTAL METHODS.....	12
2.1 Overview of Experiment.....	12
2.2 Generation of the Dispersed Particle Phase.....	12
2.3 Visualization and Quantization of Particle Field.....	14
2.4 Visualization of Carrier Gas Phase.....	15
2.5 Velocity of Particle Phase.....	17
2.6 Velocity of Gas Phase.....	19
3. Experimental Facility.....	21
3.1 The University of Missouri Shock Tube.....	21
3.2 Interface Creation Apparatuses.....	27
3.3 Planar Laser Imaging System.....	31
4. Experimental Procedure.....	32
4.1 Multiphase Interface Generation.....	32

4.2 Data Acquisition.....	35
4.3 Data Processing.....	36
5. Results.....	39
5.1 Dynamic Imaging of Air-Water Droplet Multiphase Cylinder.....	39
5.2 Particle Seeding Effects.....	41
5.3 Particle Relaxation Time Effects.....	43
5.4 Aerodynamic Breakup of Large Droplets.....	44
5.5 Mixing Width Plots.....	47
5.6 Simultaneous PIV/PLIF Imaging.....	49
5.7 PIV Analysis.....	51
5.8 Gas Phase Velocity Measurements.....	56
6. Conclusions.....	58
REFERENCE.....	59

LIST OF FIGURES

Figure	Page
1.1 Development of the Richtmyer-Meshkov Instability	2
1.2 Example wave interactions in a sinusoidal RMI.....	4
1.3 Early time development of the SDMI.....	5
1.4 Development of a circular shocked interface.....	7
2.1 Diagram of particle generation tank	13
2.2 Example interferometry setup and interferogram.....	15
2.3 Example trajectories from ACCIV analysis	20
3.1 University of Missouri Shock Tube.....	22
3.2 1D diagram of shock tube states.....	25
3.3 Example xt plot.....	27
3.4 Annular interface creation apparatuses.....	29
3.5 Contour plot of velocity magnitude through annular interface creation apparatus and shock tube test section; Velocity magnitude from PIV analysis.....	31
3.6 Nd: YAG laser with diverging optics and 4 MP ICCD camera on custom mount located at viewport.....	32
4.1 Diagram of interface introduction to test section, laser illumination of interface, and experimental images of initial state of multiphase cylinder	36
4.2 Plot of averaged intensity values from shock accelerated cylinder with threshold marked; calculated bounds of gas and particle field.....	37
5.1 Slice of test section with depiction of how an evolving interface would transit throughout the tube	40

5.2 Mie scattering image mosaic of shock accelerated cylinder with seeding density and particle relaxation effects highlighted.....	41
5.3 Fanning out of small particles in high affective Atwood number case.....	42
5.4 Aerodynamic breakup of large droplets in high relaxation time case	45
5.4 Table: Droplet breakup parameters.....	46
5.5 Mixing width plots.....	47
5.6 Simultaneous Mie scattering/PLIF images of particle and gas phases.....	50
5.7 Velocity vectors overlaid on corresponding images of shock accelerated multiphase cylinder	54
5.8 Pseudocolor plot of velocity magnitude overlaid with vector plot.....	55
5.9 Pseudocolor plot of vorticity magnitude overlaid with vector plot	55
5.10 Example PLIF image of shock accelerated multiphase cylinder and corresponding velocity vectors obtained through ACCIV analysis.....	57

Abstract

Shock driven multiphase instabilities (SDMI) are unique physical phenomena that have far-reaching practical applications in engineering and science. The instability is present in high-energy explosions, scramjet combustors, and supernovae events. The SDMI arises when a multiphase interface is impulsively accelerated by the passage of a shockwave. Complex particle-gas interactions are the driving mechanism of the SDMI. Particle effects such as lag, aerodynamic breakup, and mass, momentum and energy exchanges with the gas all contribute to the development of the instability. An experiment has been developed for studying the SDMI at the University of Missouri's shock tube facility. A multiphase interface is created and flowed into the shock tube test section where it is accelerated by the passage of a planar shock wave. Dynamic imaging of the interface was used to analyze the flow morphology. The effects of Atwood number (particle seeding), particle size, and a secondary acceleration of the interface were examined providing a qualitative and quantitative analysis of the flow. Non-intrusive flow visualization techniques such as Particle Image Velocimetry and Planar Laser Induced Fluorescence were used to obtain quantitative measures of multiphase effects. New imaging techniques were designed for the simultaneous imaging of droplet and vapor fields. Measurements of particle lag distance, carrier and dispersed phase velocity, and vorticity were made. The experimental set up and findings will be discussed in detail.

1 Introduction and Background

1.1 Applications

The shock-driven multiphase instability (SDMI) occurs when a heterogeneous multiphase field, such as a particle-seeded gaseous medium, is instantaneously accelerated by the passage of a shock wave. After acceleration, complex particle-gas interactions result in vorticity generation and multi-scale mixing. The instability presents itself across a wide range of naturally occurring and human-made systems. In high-speed combustion, the SDMI aides in the evaporation and mixing of air and liquid fuel in scramjet, pulse, and rotating detonation engines¹⁻⁸. Shock-multiphase interactions also occur in industrial devices such as steam turbines and ejector pumps^{9, 10}. In astrophysics, the SDMI is thought to play a role in the processing of circumstellar cosmic dust in supernovae and Asymptotic Giant Branch stars^{11, 12}. In volcanic eruptions, strong accelerations interact with multiphase media, producing ash ejecta in the atmosphere¹³.

1.2 Theory: The Richtmyer-Meshkov Instability

In the case of small, fast reacting particles it becomes impossible to distinguish particles from heavy gas molecules. At the limit of infinitely small particles, the system behaves as a single fluid reacting to changes in momentum at the same rate. The instability can then be treated as the single fluid, multi-species instability known as the Richtmyer-Meshkov (RM) instability. In a RM instability, vorticity develops from a misalignment between a pressure and a density gradient. This misalignment allows for the deposition of baroclinic vorticity over the interface of different density fluids. This vorticity will drive the fluid interface to grow in an unstable fashion, producing many length scales, as well as promote mixing of the species across the interface. This will result in a turbulent mixing process. A graphic of how the RM instability develops is shown below.

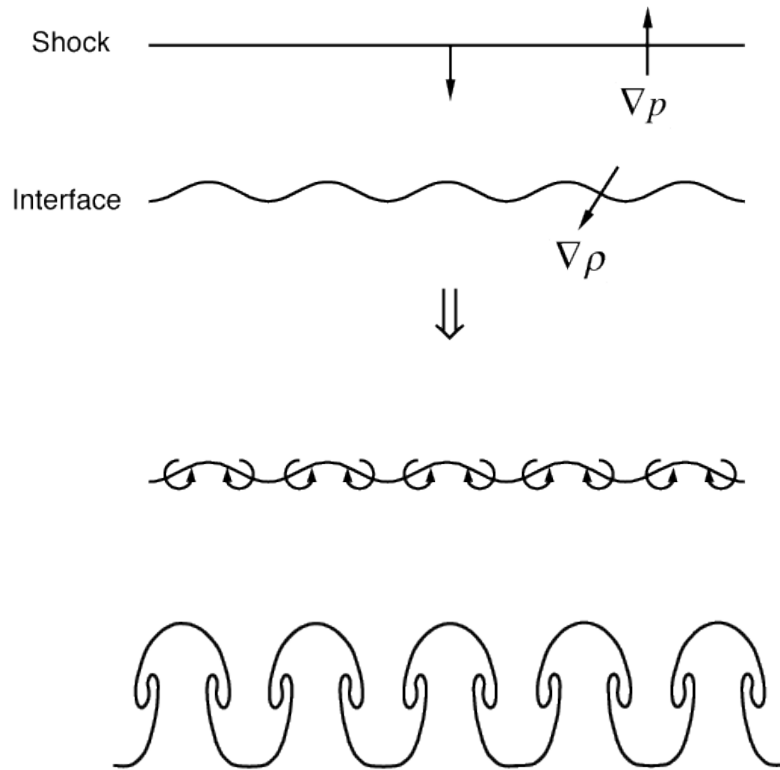


Figure 1.1 Shock interaction, baroclinic vorticity deposition, and unstable interface growth of Richtmyer-Meshkov Instability in the case of a shock propagating through a low density gas into a high density gas

Robert D. Richtmyer first mathematically examined the case of an interface between two fluids of differing densities being impulsively accelerated¹⁴. He began with the classical fluid instability problem of the interface of two incompressible fluids of differing densities being constantly accelerated by gravity. This scenario is known as the Rayleigh-Taylor instability¹⁵. The equations describing the growth of the interface are given below.

$$z = a \cos(kx) \quad (1.1)$$

$$\frac{d^2 a(t)}{dt^2} = kg(t) \left(\frac{\rho_2 - \rho_1}{\rho_2 + \rho_1} \right) \quad (1.2)$$

$$ka \ll 1 \quad (1.3)$$

Where a is the amplitude, and k is the wave number of the interface. The acceleration of the amplitude over time is then given to be proportional to k multiplied by a gravitational acceleration (g) multiplied by a ratio of the difference of fluid densities to the sum of the fluid densities. This ratio is commonly referred to as the Atwood number (A). In the model equations, the subscripts 1 and 2 denote fluids on the bottom and top of the sinusoidal interface respectively.

$$A = \frac{(\rho_2 - \rho_1)}{(\rho_2 + \rho_1)} \quad (1.4)$$

Richtmyer was interested in how the interface would evolve if the acceleration was not constantly applied, but rather impulsively. Richtmyer modified the equations from Taylor's model to describe such a scenario, creating his impulsive model. Considering the limit of an impulsive acceleration (shock wave), Richtmyer extend his model to incorporate the effects of compressibility. The equations for the interface dynamics during a shock interaction were then provided. They are displayed below.

$$z = -w_1 t + a_1(t)e^{ikx} \quad (1.5)$$

$$z = a_0(t)e^{ikx} \quad (1.6)$$

$$z = w_2 t + a_2(t)e^{ikx} \quad (1.7)$$

In these equations, w is the wave speed of the shocks where the subscripts 1, and 2 represent transmitted and reflected shocks respectively. Additionally, $\cos(kx)$ is abbreviated here with e^{ikx} from the Euler identity. The three equations here represent the positions of transmitted and reflected shocks, as well as the position of the fluid interface. Region 0 is the un-shocked region of gas just ahead of the transmitted shock front.

Region 1 is the gas that has been accelerated by the transmitted shock front. Region 2 is the gas that has been shocked by both the transmitted wave and the reflected wave. A graphic of the interaction is given below.

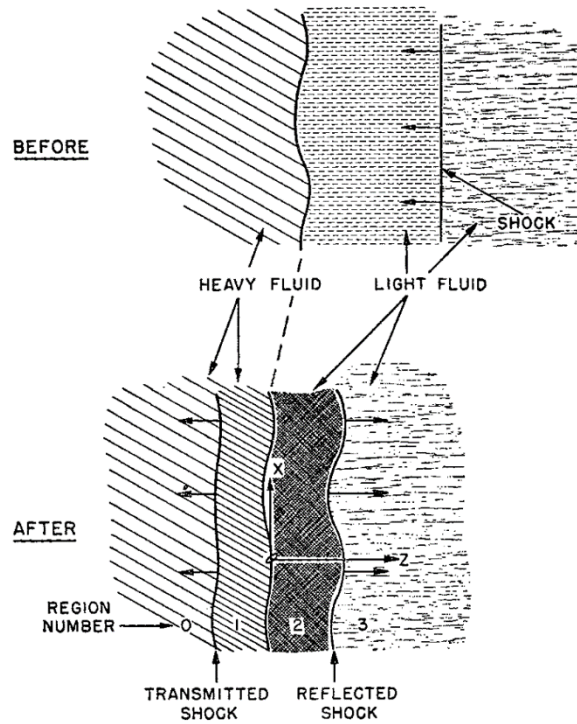


Figure 1.2 From Richtmyer's Impulsive Model¹⁴. Interaction of a shock wave with an interface possessing a sinusoidal initial perturbation

It should be noted that Richtmyer's analysis was done in the framework of a shock propagating initially through a low density (light) gas into a high density (heavy) gas.

The RM instability can develop from the reverse scenario, however the vorticity deposition will be reversed. The instability described by Richtmyer was later validated by E.E. Meshkov through shock tube experimentation¹⁶ and the instability was eventually named after the two scientist.

1.3 Theory: The Shock-Driven Multiphase Instability

Many of the wave interactions and interface dynamics of the RM instability can be observed in the case of a particle field being impulsively accelerated (SDMI). However, the SDMI evolves from gradients in particle-gas momentum transfer and not a deposition of baroclinic vorticity. In a simple example, the SDMI evolves from interactions of a shock wave with a sharp boundary of a particle field. Figure 1.3 shows an example evolution of an SDMI created by a circular field of particles. As the shock passes through the interface the gas reacts immediately, jumping to the post shock conditions, while the particles are initially unaffected. The particles equilibrate with the gas through mass, energy and momentum transfer appearing as sources in the gas. At the edge of the particle field there will be a strong gradient in these sources; between the particle laden field and surrounding clean gas. The gradient in momentum transfer will result in velocity gradients (shear) between the clean and particle laden gas, resulting in vorticity production at the interface¹⁷⁻¹⁸.

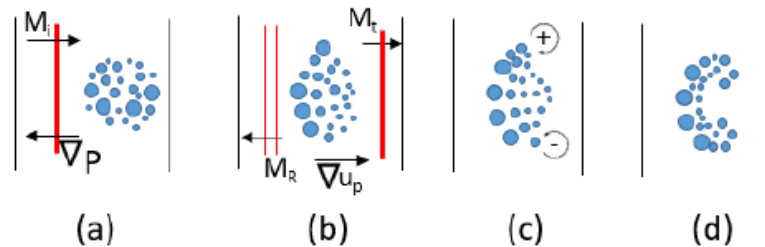


Figure 1.3 Early time development of the SDMI

For large particles, which do not equilibrate immediately with the gas, the deposition of vorticity is more complex and occurs over a finite amount of time. As large particles lag behind the gas, they deposit vorticity over their path. This appears as a

vorticity source, which advects through the gas. The multiphase source term in equation 1.8 accounts for this effect. The multiphase source term depends on the momentum transfer from the particles, where F_k is the force on the gas determined by particle drag. A thorough derivation and definition of this term is displayed in the 2017 paper from Dahal and McFarland over the subject¹⁸.

$$\partial_t \frac{\omega_i \omega_i}{2} + u_{g,j} \partial_j \frac{\omega_i \omega_i}{2} = \left[\omega_i \frac{1}{\rho_g} \varepsilon_{ijk} \partial_j \rho_g \partial_k P \right]_{\text{baroclinic}} + \left[\frac{1}{\rho_g \mathcal{E}} \omega_i \varepsilon_{ijk} \partial_j F_k \right]_{\text{multiphase}} + \dots \quad (1.8)$$

As this source advects through the flow it deposits vorticity, which competes with previously deposited vorticity in the gas. The result is that as particles increase in size, the vorticity that persists in the gas phase decreases. The multiphase source term in the enstrophy equation shows this effect as it depends on the alignment between the vorticity and the vorticity source and will decrease as particles lag further behind the flow. Equation 1.8 shows the baroclinic term related to the RM instability and the multiphase source term related to the SDMI coinciding. This indicates that the terms are not exclusive, and both RM-like and SDMI-like hydrodynamic behavior can be observed in a single system that possesses both a density gradient and multiphase source.

To create the SDMI, three ingredients are necessary: an impulsive acceleration, quantified by the shock wave Mach number M , a perturbed multiphase field, and a misalignment between the shock wave and the gradients in the multiphase field. The misalignment is often quantified by a ratio of length scales parallel and perpendicular to the shock acceleration. Complex interfaces can be decomposed into a Fourier series using the amplitude and wavelength of each mode, as is done in many hydrodynamic problems

(RM. Rayleigh-Taylor, Kelvin-Helmholtz, etc...). In the case of a sphere or circle, the ratio is constant, but the interface development is unique as it develops from shock interactions with two interfaces (the upstream and downstream edges of the sphere or circle). A depiction of this happening in a circular RM instability scenario is shown below.

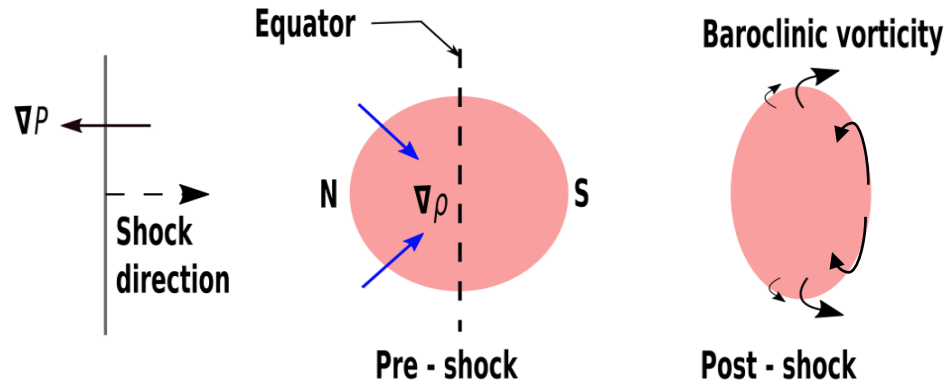


Figure 1.4 Shock interaction and baroclinic vorticity deposition of a shock accelerated circular interface. The baroclinic vorticity is initially departed in one direction until the shock crossed the mid-point of the circle. At the mid-point the vorticity deposition is greatest, and after this, the vorticity deposition is reversed

A hydrodynamic instability (HI) can be generally defined as an unstable fluid motion that works to drive the flow field to a turbulent state. Typically, HI's are created experimentally by accelerating the interface of two dissimilar fluids that has an initially defined perturbation. For impulsive HI experiments, a shock front is passed through an interface for the acceleration. For this reason, various methods have been developed for generating shock accelerations in hydrodynamic instability (HI) experiments. In high-energy experiments, a laser ablation-driven method can be used for small-length scale experiments^{19, 20}. A blast wave (unsupported shock front) generated from exothermic chemical reactions can be used for larger scales²¹. For lower energy experiments, a shock tube can be used to generate a shock front. A mechanically driven shock tube works by

rapidly releasing a stored volume of high pressure gas into a region of lower pressure. This can be done by rupturing a diaphragm^{22, 23} or using a rapid release valve²⁴.

For a shock tube that is sealed by an end wall, multiple accelerations from incident and reflected waves can occur. These subsequent accelerations are common in many applications of the SDMI where multiple shock and expansion waves intersect a multiphase field. These additional accelerations impart new energy into the system, altering the initial flow morphology. A partially evolved instability (from the initial acceleration) presents a wider range of length scales where energy can be added by a secondary acceleration. This creates additional mixing, smaller length scale features, and helps the flow to develop a turbulent energy cascade²⁵⁻²⁷. These complex accelerations can be beneficial when increased mixing is desired (e.g. a combustion process) and are necessary to explain the formation of some structures in astrophysical events²⁸.

A perturbed multiphase flow field, required for the SDMI, can be created in a simple manner using the interface between clean and seeded gases. Such interfaces are employed in RM experiments as well, using fluids of differing densities. Thin membranes have been used to create gas interfaces either in planar or spherical (bubble) form^{29, 30} but result in undesirable membrane fragments in the flow. Sine-wave like perturbations have been created by oscillating a membrane-less interface before shocking it^{31, 32}. Inclined interfaces have been created by tilting a shock tube at an angle, and shear and buoyancy-driven interfaces have been used to create turbulent-like multimodal interfaces³³⁻³⁶. A simple cylindrical interface (used in this work) is created by flowing a laminar jet through a shock tube. A series of connected cylindrical interfaces can also be used to create an interface in horizontal and inclined shock tubes³⁷⁻⁴⁰.

To quantify the strength of the perturbation in the multiphase flow field, RM instability theory is borrowed where the density gradient is quantified by the Atwood number. To relate this to the SDMI, we can return to the simple case of infinitely small particles where the multiphase source terms will scale directly with the particle mass loading of the multiphase mixture. The effective density brought about by particle seeding is $\rho_e = (m_{\text{particles}} + m_{\text{gas}})/V_{\text{mixture}}$. ρ_e can then be used to calculate an effective Atwood number, A_e for the system. This number can be used in place of the Atwood number to modify the RM theory to account for fluid and particle density effects in the case of small fast reacting particles⁴⁰.

$$A_e = \frac{(\rho_{e2} - \rho_{e1})}{(\rho_{e2} + \rho_{e1})} \quad (1.9)$$

For larger particles, it is necessary to quantify the effect of finite equilibration times. This is done using relaxation times for the various modes of particle-gas coupling (mass, energy, and momentum)⁴¹. The velocity relaxation time, τ_v (equation 1.10, where m_p is the mass of a single particle, d is the diameter, and μ_g is the gas viscosity), is most important to the SDMI. This term determines the duration of advection of the multiphase source term and its vorticity deposition. The impact of this time depends on the hydrodynamic growth time scale. For our example case of a circular particle field, we use the shock transit time (time taken by shock wave to traverse the interface) $t_c = D/w_i$ where D is the interface diameter and w_i is the incident wave speed. The effect of the momentum relaxation can then be quantified by the non-dimensional velocity relaxation time, $\tau_v = t_v/t_c$. As τ_v increases, the vorticity deposition is damped and the interface development becomes increasingly driven by particle lag. The threshold for when

relaxation time effects become considerable has been estimated to be approximately $\tau_v > 0.1$.

$$t_v = \frac{m_p}{3\pi d \mu_g} \quad (1.10)$$

1.4 Droplet Effects

Additional multiphase effects need to be considered for liquid particles (droplets). Droplets are deformable and may take on different shapes altering their drag or may breakup into smaller droplets^{42, 43}. For multiphase flows, breakup occurs in different regimes depending on the Weber number, $We = \rho_g (u_g - u_p)^2 d_p / \sigma$, where u_g , u_p , d_p , σ are the gas and particle velocities, droplet diameter, and surface tension respectively. Droplet breakup typically occurs above a critical weber number⁴⁴ of ~ 12 . Droplet breakup is also governed to an extent by the Ohnesorge number, defined as the ratio of viscous to inertial and surface tension forces. The Ohnesorge number is defined as: $Oh = \mu_p / \sqrt{\rho_p d_p \sigma}$ where μ_p is the dynamic viscosity of the droplet, ρ_p is the density of the droplet, and σ is the surface tension of the droplet⁴⁵. Additionally liquids may evaporate; producing mass transfer between the phases and altering both energy and momentum transfer. The effect on energy coupling is largely due to the latent heat of vaporization of the particle material. This manifests as an evaporative cooling effect in the particle vicinity that alters the density of the gas. Evaporation effects do not strongly alter the interface development after incident shock, but can strengthen the effective Atwood number, leading to a stronger instability from a subsequent acceleration^{46, 47}. As we use liquid particles in this work, we will refer to them as both droplets and particles, reserving the term droplet for multiphase effects pertaining to liquid particles.

1.5 Previous and Related Works

The previous work on SDMI is limited, and it is difficult to attribute the discovery of a particle seeding-induced instability to just one group. Physical occurrences integral to the development of the SDMI have been studied extensively by previous researchers, but the development of a particular hydrodynamic instability was not considered^{48, 49}. Vorobieff et al were perhaps the first group to investigate a general instability produced purely through particle seeding⁴⁰. The group termed the instability the Particle Lag Instability (PLI) initially, but have more recently adopted the term SDMI. Interest in the field has increased, and new experiments⁵⁰ and simulations⁵¹⁻⁵⁴ into particle-induced instabilities have been conducted for various applications.

The experiments performed by Dr. Vorobieff's group are the most relevant to this work, and share many similarities. This work studied the mixing from a shock-driven cylindrical multiphase interface seeded with non-evaporating micron-sized dipropylene glycol droplets, and first identified the multiphase effects as being unique from and RM instability. This work expands upon these efforts in many ways.

Now that sufficient background information has been given, the following sections of this report will describe the University of Missouri's shock tube facility and the new multiphase experiment. Our results highlighting the effects of varied particle relaxation times, particle seeding density, secondary accelerations, and particle breakup will be presented and discussed.

2 Experimental Methods

2.1 Overview of Experiment

This report details an experimental study of the SDMI carried out at the University of Missouri's shock tube facility. In our experiments, a shock tube is used to generate a shock wave by rapidly releasing a volume of high pressure gas into a region of low pressure. This is accomplished by storing high pressure gas in a driver section separated from the rest of the tube by a diaphragm. When the diaphragm is ruptured the pressure rapidly equalizes, generating the shock. A perturbed multiphase flow field can be created in a simple manner using an interface between clean and seeded gasses. The simple cylindrical interface used in our work is created by flowing a laminar round jet of liquid particle seeded air or nitrogen into the shock tube test section. Several non-intrusive, planar laser based imaging techniques were used to qualitatively and quantitatively study the interface's development before and after shock acceleration. An overview of relevant experimental techniques used in this endeavor follows.

2.2 Generation of the Dispersed Particle Phase

There are many methods that can be used to create a multiphase flow field. Precisely sized solid particles of various materials can be purchased and dispersed. For liquid particles (droplets) there are several methods available for atomizing a liquid and dispersing it into a gas; effectively creating an aerosol⁵⁵. Pressure and rotary atomization methods use the momentum of the liquid, while two-fluid atomization methods use the momentum of the gas to shear a liquid, breaking it into droplets.

To create the particles for the multiphase flow field used in this work, ultrasonic and piezoelectric atomizers were used. Ultrasonic atomizers use high frequency oscillating diaphragms to pulse acoustic waves through a fluid. This causes capillary waves to form on the surface of the liquid that increase in amplitude. Once a certain amplitude is reached, the waves will form upward jets that break up into droplets⁵⁶⁻⁴⁸. The equation that predicts the droplet diameter formed from a viscous fluid being forced by waves at a given frequency is $d = 2\pi c(9\nu/2\omega)^{(2/3)}$. Where d , ω , ν , and c are the diameter of droplet produced, forcing frequency, kinematic viscosity, and analytically determined constant respectively.

Piezoelectric oscillating meshes produce particles by forcing a liquid through micron sized pores. The oscillatory motion of the mesh pumps the liquid through the pores and up into a gas in the form of a fine spray. The diameter of the particle produced from a vibrating orifice generator (oscillating mesh of known pore size) is given by $d = (6Q/\pi f)^{(1/3)}$. In the equation, Q is the volumetric flow rate through the orifice, and f is the frequency driving the vibration (oscillation). The benefit to ultrasonic and piezoelectric oscillating mesh atomizers is that both produce particles in a highly repeatable manner within a narrow range of particle diameters^{59, 60}. These devices are rated to produce particles of an average diameter per a given input voltage and frequency.

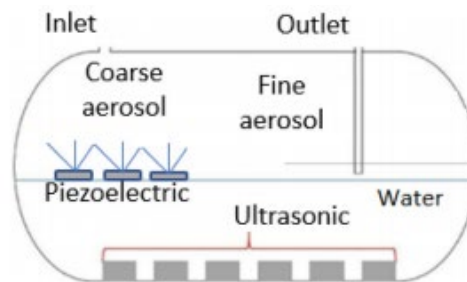


Figure 2.1 Diagram of particle generation tank with both piezoelectric and ultrasonic atomizers shown

2.3 Visualization and quantization of particle field

The size distribution of droplets can be estimated through filtration mass retention measurements using fibrous filters varying in collection efficiencies⁶¹. The droplet laden gas is passed through a series of filters decreasing in porosity. After each filter pass, the amount of mass (water droplets) retained by the filter is measured with a precision balance. The percentage of mass lost from the interface is directly related to the droplet size distribution within the interface.

A more precise measurement of particle size can be attained through laser interferometry. Laser interferometry is a visualization technique that can be used to measure individual transparent particles within a multiphase field at low particle concentrations (i.e., single particles can be isolated). The process used Mie scattering to illuminate a section of the flow with a small planar sheet of light. The particles within the interface will reflect light in the forward scattering range. A camera is used to capture this reflected light from the particles. If the image is taken so that the illuminated plane is at the correct focal distance, the reflected and refracted rays of light will interfere with each other generating a fringe pattern for each particle.

An example interferometry setup and interferogram showing fringe spacing in water droplets can be seen in figure 2.2. The equation that relates the number of fringes within a single particle to its diameter can be seen in equation 2.1, where d is the diameter, N is the number of fringes, θ is the scattering angle, α is the collection angle ($\alpha = N \cdot \Delta\theta$), $\Delta\theta$ is the fringe space, λ is the wavelength and m is the refractive index of water. More on Mie scattering and interferometry techniques can be found in the given

references⁶²⁻⁶⁴. The validity of particle size measurement techniques can be verified by comparing results with the previously given analytical equations that predict droplet formation through ultrasonic and piezoelectric atomization [more details given in Kothakapa 2017 thesis].

$$d = \frac{2\lambda N}{\alpha} \cdot \frac{1}{\cos(\theta/2) + \frac{m \sin(\theta/2)}{\sqrt{m^2 + 1 - 2m \cos(\theta/2)}}} \quad (2.1)$$

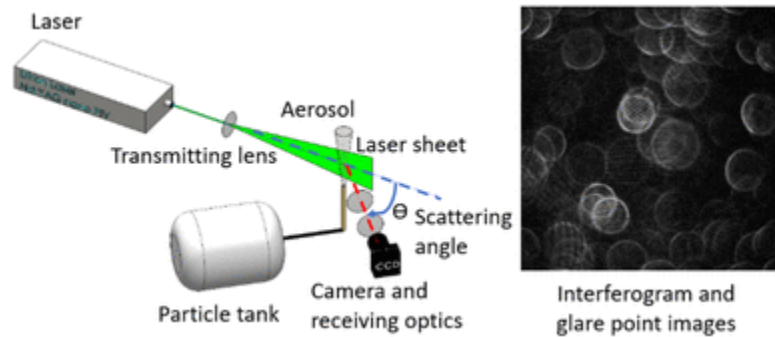


Figure 2.2 Example interferometry setup and interferogram. From Kothakapa 2017

2.4 Visualization of Carrier Gas Phase

To visualize and quantify the gas component of the multiphase interface, Planar Laser Induced Fluorescence (PLIF) imaging was utilized. PLIF is a technique that relies on the dispersal of a fluorescent compound within a flow field. A planar laser sheet at a specific wavelength is then passed through the flow to excite the tracking compound. Molecules within the compound will absorb the energy imparted by the laser sheet and jump to an excited state. The molecules within the compound dissipate this excess energy through the emission of photons; light of a longer wavelength is emitted as the system

returns to its ground state. The wavelength and intensity fluoresced back can be used to identify the position and concentration of the tagged component instantaneously.

The equation that relates fluorescence intensity and number density (concentration of fluorescent compound) is given below in equation 2.2⁶⁵. This equation assumes that the tracking fluorescent component is acetone vapor. S_b and S_c correspond to the measured background and collected signal respectively. The difference between the two is equivalent to gain or responsivity of the sensor G_i , times the efficiency of the collection apparatus η , times the population distribution function $f(T)$, the acetone number density N_{acetone} , the fluorescence quantum yield η_f , and the local laser intensity $I(x,y)$. PLIF can provide a multitude of two-dimensional flow field measurement. Some examples are: pressure and temperature measurements; density gradients; species concentrations; and velocity fields.

$$S_c(x,y) - S_b(x,y) = G_i \eta_{\text{collection}} f(T) N_{\text{acetone}} \eta_f I(x,y) \quad (2.2)$$

Acetone vapor is commonly used in PLIF experiments because of its linear relationship between fluorescence, vapor concentration, and laser power under certain conditions (isothermal and isobaric)⁶⁶. Acetone's absorption and emissions spectrums do not overlap, making the filtering out of reflected incident laser pulses a relatively simple process. Additionally, the phosphorescent behavior of acetone (a slower, non-instantaneous signal) is sufficiently quenched in the presence of oxygen.

It was mentioned that acetone maintains a linear relationship with incident laser light, concentration, and fluorescence under isobaric and isothermal conditions. For the highly dynamic pressure and temperature fluctuations that occur in a shock tube

environment, information regarding acetone's fluorescence under extreme conditions is needed. Acetone's fluorescence under conditions similar to those found in an internal combustion engine have been examined⁶⁷. The pressure range was reported to be .2-20bar and the temperature range was reported to be between 298-748 K. For reference, post shock conditions within our shock tube running at our standard Mach number of 1.66, are approximately ~3.1bar and 418 K. With a secondary shock passage, temperature and pressure can jump to ~7.9bar and 564 K respectively. Results reported from this experiment were signal intensities of acetone fluorescence under varied temperature, pressure and excitation wavelengths (248nm and 308nm). Acetone's fluorescent behavior over the specified temperature and pressure range was found. For experiments pertaining to acetone in N₂, no pressure dependence on absorption up to 20 bar at room temperature, and up to 8 bar at 698K was found.

2.5 Velocity of Particle Phase

To image the particle field, and obtain instantaneous velocity measurements, Particle Image Velocimetry (PIV) was used. PIV is a flow visualization technique that relies on the dispersal of a tracking particle within a flow field. The particles are typically small (on the order of microns) and are assumed to faithfully track the development of the flow field. The measure of a particle's ability to track a flow is the particle's Stokes number. The Stokes number is defined as

$$St = \frac{\tau_p u}{L} \quad (2.3)$$

Where τ_p is the relaxation time of the particle in flow, u is the free stream velocity of the flow, and L is characteristic length of the particle (diameter).

Once the particles are seeded into the test flow the field can be illuminated, typically by a pulsed laser or strobed LED. The illumination of the flow field causes particles to scatter light, via Mie Scattering, and this scattered light is collected by a sensor, usually a CCD camera. The illumination pulses are timed with CCD sensor activation through an external synchronizer. Images are taken in straddled frames, where each frame corresponds to an illumination pulse. If the delay between pulses is known, the exact time at which a flow field appears within an image can be determined. This can be done with microsecond precision.

The frame pairs are subdivided into smaller regions known as interrogation windows. The motion of a small group of particles is used to determine the likely displacement of interrogation windows between frames. A cross correlation algorithm is used to determine displacement vectors for individual interrogation windows. Knowing the time between laser pulses, and the displacement of windows within an image, it becomes possible to generate velocity vectors for an image set. Since the correlator works by comparing intensity signals from individual interrogation windows between frames, there is a trade-off between frame size (resolution of field) and accuracy of solution. The windows should be large enough to contain enough particles (signal intensity source) to allow for a good correlation to be found, but not so large that the particle motion between frames cannot be discerned. The time separation between frame pairs must also be considered. For a set frame size, too large of a time separation will result in large displacements of particle clusters and the calculation of a coarse, inaccurate solution. Conversely if the time separation is too small, too little displacement of particle clusters will occur and correlations will be impossible to determine. The correlation method

employed can also affect the accuracy of the solution. Direct correlators are typically more accurate but are computationally burdensome and lack the speed of Fast Fourier Transform (FFT) correlators⁶⁸.

While many factors must be considered in PIV analysis, done properly this technique can accurately produce 2 and 3-dimensional instantaneous velocity fields without the introduction of a probe such as a Pitot tube or hotwire. The vectors can be plotted over corresponding images of the flow field or as standalone vector plots. Velocity fields can also be used to obtain other quantitative measures such as flow field vorticity, circulation, Reynold stresses, and divergence⁶⁹⁻⁷².

2.6 Velocity of Gas Phase

Gas phase PLIF images can be used to create velocity fields from shock accelerated interfaces. This was done using the ACCIV method⁷³. The method works by first constructing a crude velocity field through image correlation. This crude velocity field is then used to numerically advect pixels forward and backward in time following the trajectory of the initial velocity. Uncertainties in the advection process will result in trajectories with inherent overshoots. A smooth curve is then interpolated between the two predicted trajectories creating a more realistic prediction of pixel trajectory and velocity. The process is iterated until the error (offset) between trajectories meets a convergence criteria. From the final velocity field construction, vector plots of gas velocity can be constructed. An example of the process is displayed below in Figure 2.3.

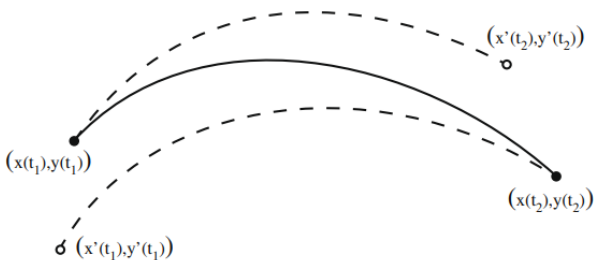


Figure 2.3 Example trajectories produced through numerical advection and interpolated path⁶³.

The technique was first developed by Assay-Davis et al for the study of Jovian atmospheric dynamics. Time separated satellite images of the turbulent atmosphere were used in the ACCIV algorithm to generate corresponding 2D velocity and vorticity fields. The technique was later adopted by shock tube researchers and applied to the study of turbulent shock accelerated planar gas interfaces⁷⁴. The resultant velocity and vorticity fields were found to be comparable to results obtained from PIV analysis and numerical simulation.

3 Experimental Facility

3.1 University of Missouri Shock Tube

our experiments were conducted at the University of Missouri's Fluid Mixing Shock Tube Laboratory (MU-FMSTL). The Facility uses a horizontally oriented shock tube with a modular design that accommodates experiments through late time development and secondary accelerations. An image of the experimental facility is presented below in figure 3.1. It is designed to support a Mach 2.75 shock wave propagating into atmospheric air with an FOS of 2. The tube is approximately 9.5 m in length and consists of 3 main sections: driver, driven, and test sections.

The driver section stores high pressure gas required for initiating the shock. It is approximately 1.5 m in length and has an OD of 10.75 inches with 1 inch thick walls made from carbon steel with an AMSE rating of 4651 psi (NPS 10 schedule 140 pipe). This is more than double the pressure of commercially available compressed gas cylinders (2200 psi). The back plate of the driver is made from 2 inch thick high-strength steel and has been tapped with several ports to allow for instrumentation and gas flow.

Pressure and temperature measurements are made in the driver using an Omega PX309 static pressure transducer and type K thermocouple. These measurements help to determine the initial conditions and are necessary to predict theoretical post shock conditions. The driver is also fitted with two valves; a fast-acting high-flow solenoid valve and slow-acting low-flow valve.

The driver is connected to the driven sections by circular flanges clamped together using a hydraulic ram system. A thin diaphragm made of polycarbonate is placed between the driver and lower pressure sections and the driver is slowly charged to a higher pressure (approximately 80% of the diaphragms rupture pressure).

An “X” shaped knife edge is placed just downstream of the diaphragm in the driven section to increase the repeatability of diaphragm failure. When the driver reaches a critical pressure, the high flow valve is activated and the diaphragm pushes against the knife edge until it is failed, releasing the high-pressure gas and initiating the shock.

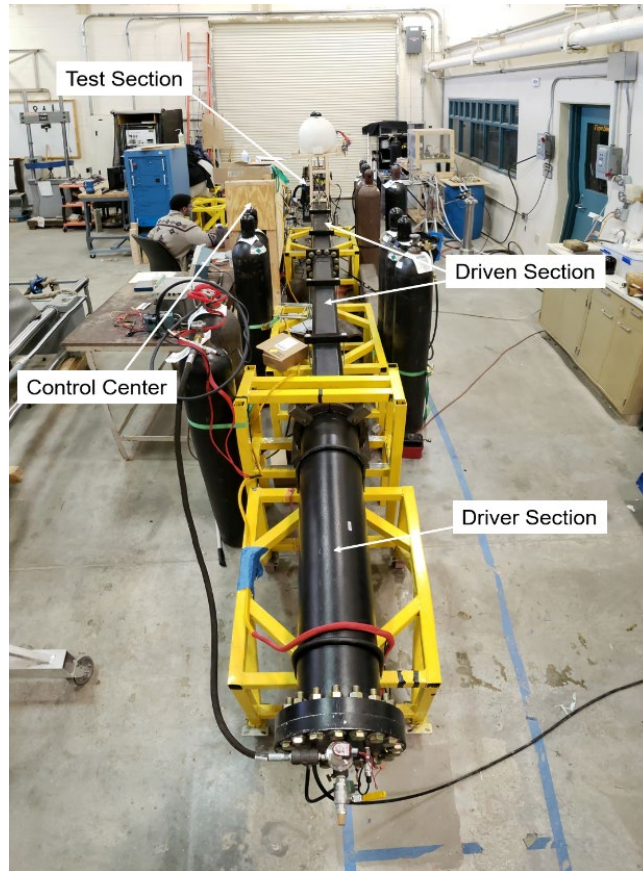


Figure 3.1 University of Missouri shock tube facility

After the diaphragm is ruptured, a series of compression waves travel down the length of the driven section where they stack into a planar shock front. The driven section is composed of two A500 carbon steel square tubes approximately 2.5 m in length. The length of the driven section allows the initial compression waves to stack into a proper shock front, and help prevent reflected expansion waves from the initial diaphragm rupture from intersecting the incident shock front.

The sections are tapped to house two PCB Piezotronics 113B series dynamic pressure transducers (DPT) spaced four inches apart. The DPTs are capacitive based and can measure pressure changes at a sampling rate of 2 MHz. These devices play a central role in the imaging process covered in the methods section of this report, as well as determining post shock conditions. The driven section is also fitted with slow acting solenoid valves that control the flow of embedding gases in the driven section upstream of the initial interface.

The test section is comprised of 3, approximately 1 m long sections made from the same A500 steel tubing used in the driven sections. The interface creation subsection houses the initial perturbed interface. It has five windows for viewing the developing interface at key times, and two 1 inch wide slots to accommodate an interface creation apparatus. Camera mounts can be attached to the view ports to support the CCD cameras used in imaging. The reshock subsection was designed with four view ports spaced for horizontal and vertical viewing of the developing interface at later times. A blank subsection can also be placed strategically within the arrangement to adjust the arrival time of reflected waves (e.g. the reflected incident wave from the test section end wall that travels upstream known as the reshock wave) or change the viewing times of window ports located in the reshock section. The windows for viewing the interface development were made from acrylic and sealed with a silicone based epoxy. The back plate of the test section is housed with a thermocouple and pressure transducer as well as a low flow valve to control the flow of embedding gases downstream of the initial interface. The back plate also features a centrally located Sapphire glass window which allows for the introduction of laser light both in the visible (532 nm) and UV (266 nm) range.

1D gas dynamics can be used to predict the position of the interface at a given time after shock acceleration. 1D shock tube relations can be used to predict state properties within the tube after wave interactions. The 1D shock tube relations are given below.

$$\frac{P_4}{P_1} = \frac{P_2}{P_1} \left\{ 1 - \frac{(\gamma_4 - 1) \left(\frac{a_1}{a_4} \right) \left(\frac{P_2}{P_1} - 1 \right)}{\sqrt{(2\gamma_1 [2\gamma_1 + (\gamma_1 + 1) \left(\frac{P_2}{P_1} - 1 \right)])}} \right\} \quad (3.1)$$

$$\frac{T_2}{T_1} = \frac{\frac{P_2}{P_1} \left(\frac{\gamma + 1}{\gamma - 1} + \frac{P_2}{P_1} \right)}{1 + \frac{\gamma + 1}{\gamma + 2} \left(\frac{P_2}{P_1} \right)} \quad (3.2)$$

$$\frac{\rho_2}{\rho_1} = \frac{1 + \frac{P_2}{P_1} \left(\frac{\gamma + 1}{\gamma - 1} \right)}{\frac{\gamma + 1}{\gamma + 2} + \left(\frac{P_2}{P_1} \right)} \quad (3.3)$$

$$\frac{P_5}{P_4} = \frac{(3\gamma - 1) \left(\frac{P_2}{P_1} \right) - (\gamma - 1)}{(\gamma - 1) \left(\frac{P_2}{P_1} \right) + (\gamma + 1)} \quad (3.4)$$

$$W = a_1 \sqrt{\left(\frac{\gamma + 1}{2\gamma} \right) \left(\left(\frac{P_2}{P_1} - 1 \right) \right) + 1} \quad (3.5)$$

$$M = \frac{W}{a_1} \quad (3.6)$$

Additionally a diagram of the states described equation is given in figure 3.2.

The initial state of the shock tube is represented by states 1 and 4, where state 1 is the quiescent gas in the driven and test sections and state 4 is the pressurized driver section. The two states are separated from each other initially by the existence of a barrier. At time $t=0$, this barrier is removed (in our case, the rupturing of a diaphragm), and the high pressure gas stored in the driver is released. This release of high pressure gas

into lower pressure regions generates the shock front. The sharp rise in state properties behind a shock front, sometimes referred to as “jump” conditions, are denoted by state 2.

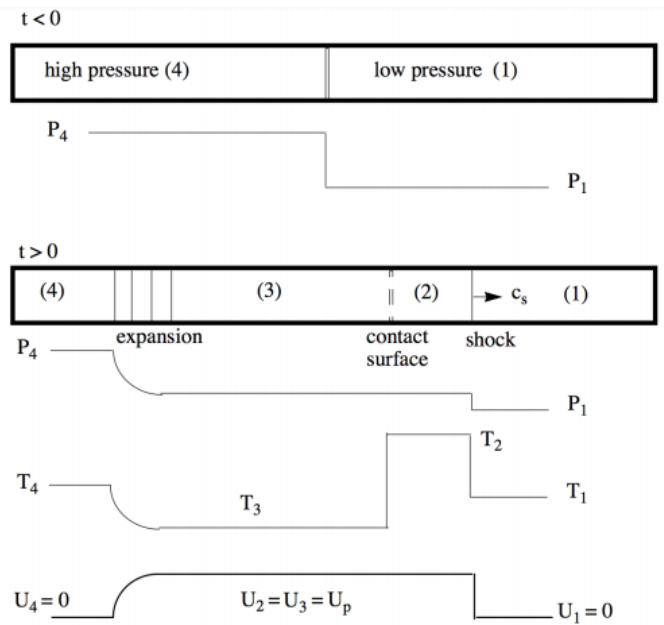


Figure 3.2 1D diagram of shock tube states

The removal of this barrier will also generate a series of expansion waves that traverse the tube initially in the direction of low to high pressure. These waves have the effect of lowering the state properties of the initially high pressure driver gas, and create a new state denoted by state 3. Not pictured in the diagram, but captured in equation 3.4 is the condition of reshock. Reshock occurs when an incident shock wave is reflected off of the solid boundary of the shock tube end wall and propagates back into state 2. This will cause an additional sharp rise in properties and bring about a new state denoted by state 5.

This 1D shock tube analysis is of course a simplification of actual dynamic events occurring in an active shock tube environment. The equations predicting the states assume the working gasses to be ideal, calorically perfect gasses (gamma is constant),

and don't account for reflections and refractions of waves at interfaces. Additionally, this analysis only considers a small number of wave interactions. In reality, an infinite number of wave interactions will occur as the system approaches its equilibrium state.

There are several numerical tools that can be used to more realistically depict conditions and wave interactions inside of a shock tube. Position-time (x-t) plots can be generated using a method of characteristics approach. In this analysis, characteristic curves are determined utilizing the method of characteristics, and plotted on an x-t axis. The curves can give immediate information on the position, time, and velocity of waves traversing the tube. Points of intersecting lines represent the intersection of wave fronts. The equations that must be satisfied in this analysis are

$$J^+ = u + \int \left(\frac{dP}{\rho a} \right) = \text{const}^+ \quad (3.7)$$

$$J^- = u - \int \left(\frac{dP}{\rho a} \right) = \text{const}^- \quad (3.8)$$

Which for an ideal calorically perfect gas reduce to

$$J^+ = u + \frac{2a}{\gamma-1} \quad (3.9)$$

$$J^- = u - \frac{2a}{\gamma-1} \quad (3.10)$$

Where J is the equations of the characteristic curve and the "+" and "-" represent right and left traversing waves. At points of intersections the following must be true

$$a = \frac{\gamma-1}{4} (J^+ - J^-) \quad (3.11)$$

$$u = \frac{1}{2} (J^+ + J^-) \quad (3.12)$$

An example x-t plots for the case of a Mach 1.66 shock wave driven by nitrogen gas into atmospheric air is shown in figure 3.3.

In this diagram, $x=0$ represents the location of a barrier initially separating high and low pressure regions. The dark curves to the right of $x=0$ represent the incident and reflected shock front. The initial expansion fan is depicted as the lighter curves traveling left of $x=0$ initially before reflecting and traveling in the positive x direction. At each wave-wave interaction, there will be corresponding reflected and transmitted waves, also depicted as lighter curves. The red lines represent the interface of air and nitrogen as well as pre and post shocked air.

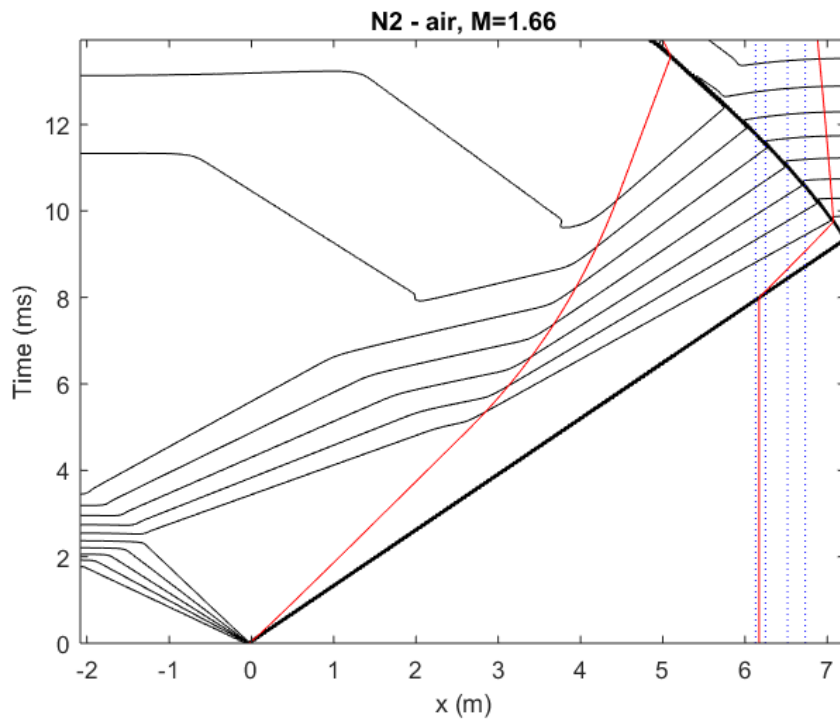


Figure 3.3 Example $x-t$ plot with conditions similar to those used at the Missouri Shock Tube facility

3.2 Interface Creation Apparatuses

The apparatus used to make the cylindrical multiphase interface consists of a flat aluminum plate with a centrally located shunt attached to a hollowed aluminum block

with a concentric hole as well as side ports for the entrance of a protective jacket gas. To mix acetone vapor into the flow for PLIF imaging, a custom vapor seeding device was designed. The device consists of a heated pressure vessel that can store liquid acetone at a regulated temperature. The container is constructed from 3 major aluminum pieces: a 3 inch OD, 12 inch long pipe with a 1/8th inch wall thickness; two 6 inch diameter, 1/2 inch thick aluminum discs. O-ring grooves were cut into the discs, as well as tapped ports for the introduction of temperature regulating instruments and gas flows. Through holes were also drilled into the disc so that threaded rods could be used to seal the container. Rigid PTFE O-rings were used to seal the pipe to plate connections. PTFE O-rings were chosen because they are chemically resistant to acetone. Acetone is a powerful organic solvent; plastic or rubber O-rings would rapidly dissolve if directly exposed to acetone liquid or vapor. Nitrogen gas is slowly bubbled through the liquid acetone creating a saturated vapor. This vapor is then mixed into the test flow at a specified volumetric flowrate.

Digital mass flow controllers meter the gas flow through the apparatuses. The valves controlling all flows into the shock tube are controlled through a LabVIEW program paired with National Instruments controls and data acquisition hardware. A PID controller is also programmed into LabVIEW that works as a thermostat for the vapor seeder. The control loop takes in temperature data from a type K thermocouple probe inside of seeder. A 50 watt cartridge immersion heater is cycled on and off until the readout temperature matches the set point temperature.

A crucial part of this experiment is the creation of a laminar, dynamically stable initial interface. Any turbulent or intermittent motions within the initial multiphase cylinder will be greatly amplified by the passage of the shock wave and will drastically

alter the development of the instability. For repeatability in experiments, a stable cylinder must be created and introduced into the test section before each run. This can be a challenge to achieve, as many factors go into the stability of a gas jet. Shearing of the initial interface can produce sinusoidal oscillations of the flow field or cause small vortices to form at the edges of the cylinder. Even slight pressure gradients or fluctuations present in the driven and test sections can tilt or bend the initial cylinder. Condensation and wall collisions can cause droplets to build up along the piping of the apparatus which will obstruct the flow.

To determine the best method for creating a dynamically stable initial interface, the flow of gasses through the interface creation apparatus and into the test section was examined. This examination was done through a parametric CFD study of flow through a 2D model of the annular interface creation apparatus and test section. This study was conducted through RANS modelling in the commercial CFD package ANSYS Fluent.

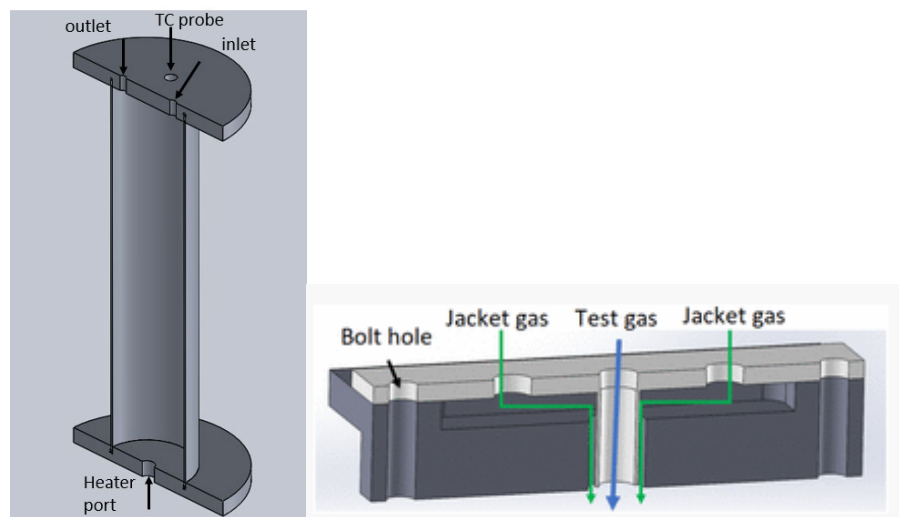


Figure 3.4 Annular Interface Creation Apparatus and Vapor Seeder models

A 2D domain scaled to the dimensions of the cross section of the apparatus, connecting pipes, and test section of the shock tube was created and meshed. An inlet mass flow rate was prescribed and pressure outlet were placed at the appropriate locations. A no slip wall conditions was placed at the bounding walls. A pressure based solver using a second order upwind scheme was used to solve the governing equations. The fluid initialized in the domain was nitrogen gas at standard conditions. To simulate the test gas, nitrogen gas with an altered density was used. The density was raised to 1.4193 kg/m³ to create an Atwood number of ~ 1.1 with the surrounding standard nitrogen of the domain. The flowrates passed through the domain were prescribed based upon achievable experimental flow rates, which are limited by the range of the mass flow controllers. Reynolds numbers for the flow through the apparatus were calculated, and used to make sure the flow would be well under the critical Reynolds numbers for pipe and free shear flows.

The simulations were transient and run until no appreciable change in the flow field dynamics could be discerned (steady state). The resolution of the mesh was varied to determine grid dependency and the trade-off between resolution and computational time. The study looked at the effects volumetric flowrate, geometries of inlet into test section and test section outlet, and the use of a protective jacket gas. Pseudocolor plots of velocity magnitude and species concentrations of the test and surrounding gasses were used to determine stability of results. It was found that the most stable interface for the current geometry of the annular device and shock tube ports was achieved when test gas flow rates between 4-6 standard liters per minute (SLM) were used without a jacket gas. These results were then compared to and validated by creating these conditions

experimentally. Experimental images of the interface at 4 SLM and corresponding velocity data obtained from PIV were examined.

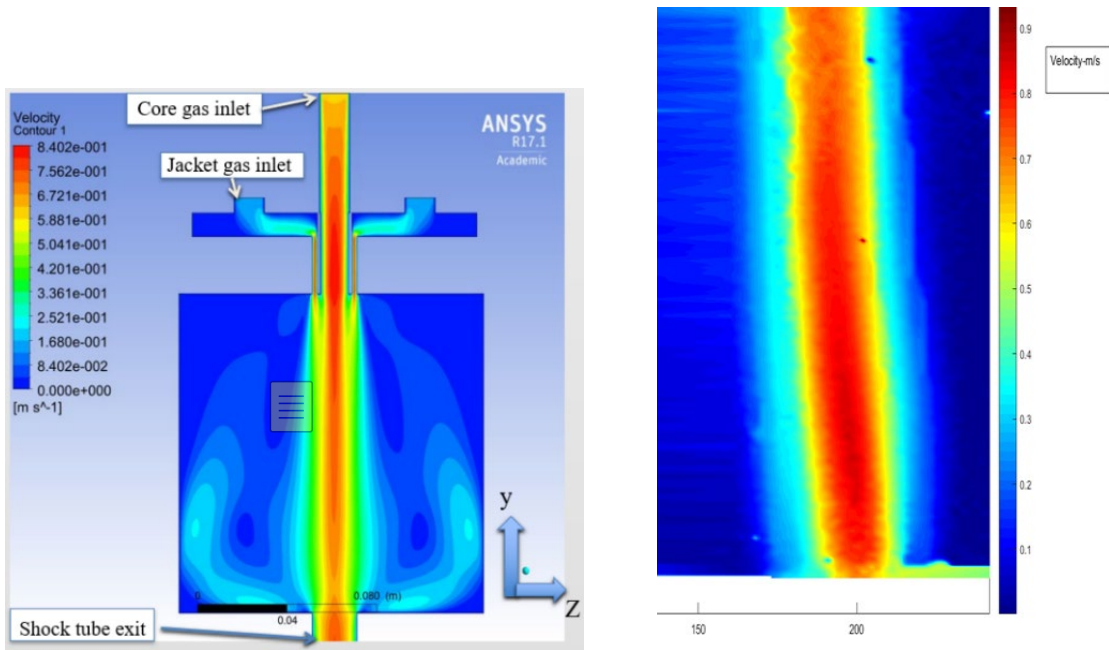


Figure 3.5 Contour plot of velocity magnitude through annular interface creation apparatus and shock tube test section (left), Velocity magnitude from PIV analysis (right)

3.3 Planar Laser Imaging System

The laser diagnostics system for our facility features a dual cavity Nd: YAG pulsed laser producing 200 mJ at 532 nm and 40 mJ at 266 nm simultaneously per pulse. A series of cylindrical and spherical lenses are used to diverge the laser beam into an optically thin sheet used for interface illumination. UV fused silica lenses are used when the transmission of UV light is required (PLIF experiments). 29 MP and 4 MP TSI ICCD cameras are used for imaging. The cameras are fitted with either 50mm F1.8 or a 50mm F1.2 Nikon lenses and a series of macro lenses for focusing. For PLIF imaging, an OD 4 notch filter centered at 532 nm is used to separate the fluorescence signal from incident and reflected 532 nm laser light. For simultaneous PIV/PLIF experiments, a narrow band

pass filter with a CWL of 532 nm is used to filter fluorescent signals from the PIV camera. An external synchronizer is used in conjunction with the TSI software 4G Insight to control the timing of laser illumination and ICCD camera sensor activation.



Figure 3.6 Nd: YAG laser with diverging optics (left), 4 MP ICCD camera on custom mount located at viewport (right)

4 Experimental Procedure

Our experimental procedure consists of three major parts: interface creation, shock wave generation and planar laser imaging (data acquisition), and data post processing. These processes will be described in this section in the order which they occur during a typical experiment.

4.1 Multiphase Interface generation

To create the multiphase interface, liquid particles (acetone or water) are entrained into the test gas flow (nitrogen or air). Particles are generated in a sealed tank by commercially available ultrasonic or piezoelectric atomizers. Ultrasonic atomizers produce fine particles ($d \sim 1.7 \mu m$) and are placed under the liquid bath, while the piezoelectric atomizers are used to create larger particles ($d \sim 10.7 \mu m$) and are placed on

the surface of the bath. A series of custom mounts have been design to hold the piezoelectric devices in place. Gas flow is metered into the tank by and Aalborg digital mass flow controller and is entrained with the particles.

For PLIF imaging, nitrogen saturated with acetone vapor at approximately 25 C is mixed into the flow at ~11 percent by volume. This is done by slowly bubbling metered nitrogen gas through the vapor seeder and introducing the saturated flow into the test flow after it has exited the particle tank, but before it enters the test section. For experiments involving water particles, acetone vapor allows for the tracking of the gas phase. For experiments utilizing acetone particles, acetone vapor is mixed into the test gas both as a tracer and to prevent early evaporation of acetone particles.

Both liquid and gaseous acetone will fluoresce when exposed to a significantly intense source of UV light. To understand how this would affect experiments involving both liquid acetone particles and acetone vapor, a set of 100 images each of a pure acetone cylinder and a cylinder comprised of acetone particles and vapor were taken and compared. It was found that on average, interfaces comprised of pure acetone vapor had a fluorescence signal that was ~6 percent brighter than an interface comprised of acetone vapor and particles. This was in accordance with theory⁵⁶. The equation which predicts the fluorescent intensity of a saturated volume of gaseous acetone normalized by incident excitation intensity is

$$\frac{S_v}{I_o} = \sigma_v N_v \left(\frac{t}{t_{ref}} \right)^2 \quad (4.1)$$

Where S_v is the vapor signal, I_o is the intensity of the excitation source, σ_v is the absorption cross-section of the vapor, N_v is the number density of the vapor, and t is the

sheet thickness of the excitation source (laser sheet). The equation which predicts the fluorescent signal from a droplet of liquid acetone is

$$\frac{S_d}{I_o} = \frac{\pi d^{3-n} \left[1 - \frac{\exp(-K_d d^n)}{3} \right]}{2} \left(\frac{t}{t_{ref}} \right)^2 \quad (4.2)$$

Where S_d is the droplet's signal, d is the droplets diameter, n is the index of refraction, and K is the absorption coefficient. Taking property values of liquid and gaseous acetone, taking t/t_{ref} to be unity (laser sheet thickness was not varied), and scaling equation 4.2 by the number of liquid acetone particles required for an A_e of ~ 0.025 (used in multiphase acetone particle-vapor experiments in this work), it was found that the ratio of normalized droplet to vapor signal was ~ 0.045 . This suggests that only 4.5% of a combined signal from a multiphase acetone vapor-particle mixture can be attributed to the liquid phase alone.

Additionally, the vapor signal overwhelms the droplet signal do to the strong absorption of incident laser light by liquid particles. This can be seen from equation 4.2 as the absorption coefficient, K , in the numerator of the first term is in the negative exponent and scaled by the diameter of the droplet to the power of the refractive index. Taking an example of a fixed volume filled with acetone droplets and vapor, as the number of droplets in the volume increases, the expected fluorescent signal intensity would decrease in value. Returning to our experimental imaging of such a system (cylinder of pure acetone vapor versus a multiphase acetone cylinder), it reasons that the pure vapor signal would be fractionally brighter than the signal from the multiphase case as was found in our experiments.

4.2 Data Acquisition

Prepared multiphase mixtures exit the mixing tanks and travel through a system of tubing and pipes until they exit into the shock tube test section in the form of a laminar round jet. The driver section is slowly pressurized to its target pressure by opening the slow fill valve. Once this target pressure is reached, the diaphragm is dynamically ruptured by opening the fast acting high flow valve sending the shock front toward the test section.

The imaging process is triggered by the incident shock passing the first DPT. The signal from the shock passage is sent through the NI hardware and triggers the LabVIEW program to acquire data and send a trigger to the laser synchronizer. The synchronizer triggers the laser pulses and CCD camera sensors to become active. The timing delays are determined by 1D gas dynamics and correspond to times at which the interface will be in the field of view of a camera.

The 29 MP camera was used to take a series of images tracking the development of a shock accelerated interface comprised of air and water particles of varying size and seeding density. The 29 MP camera was also used for PLIF imaging in experiments where gas effects were examined. The PLIF signal is comparatively dim to other light sources present in the shock tube test section during experiments. This is due to the fact that a low concentration of acetone vapor is mixed into the interface to prevent a large density gradient between the test gas and surrounding clean gasses. Additionally, the 266 nm UV light that is used to excite the acetone vapor is 20% as energetic as the 532 nm light that is used in PIV imaging. To account for this difference in signal intensities, the 29 MP camera is fitted with the F1.2 lens at its widest aperture setting and pixels are

digitally binned 2x2. This allows for the maximum amount of fluorescent light to be detected by the camera's CCD sensor. The 532 nm notch filter is used to filter any incident, reflected, or scattered 532 nm laser light present in an experiment. The 4 MP camera is used for PIV and general imaging of the particle field and is set to a tight aperture to prevent unwanted detection of the fluorescent signal in simultaneous PIV/PLIF experiments.

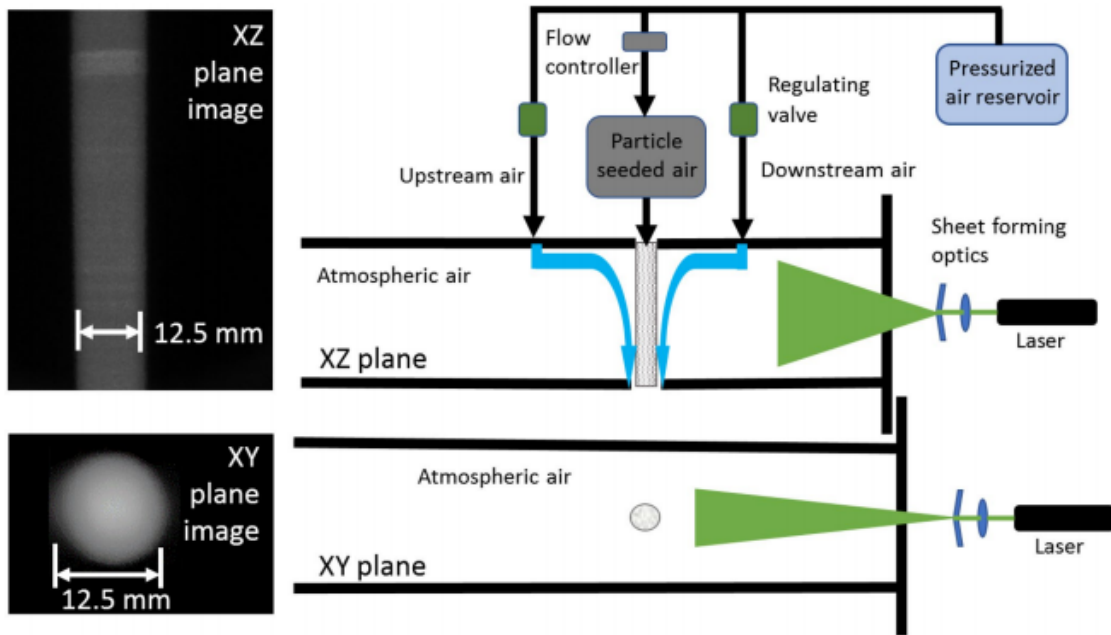


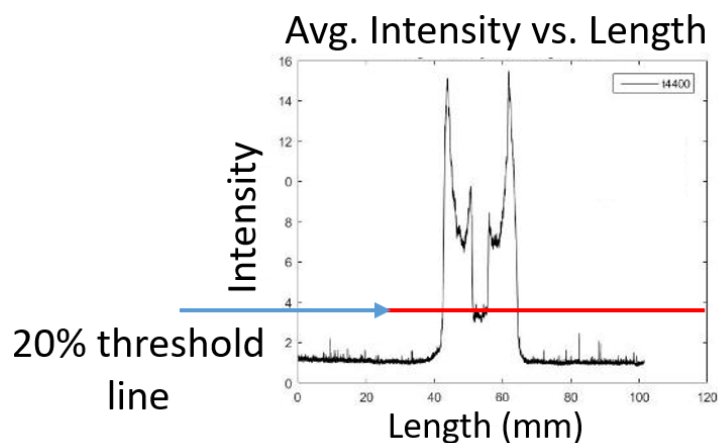
Figure 4.1 Diagram of interface introduction to test section, laser illumination of interface, and experimental images of initial state of multiphase cylinder

4.3 Data Processing

Prior to experiments, the cameras used in imaging are calibrated and focused to ensure crisp high-resolution images are captured each time. This is done by placing either a targeting block of known metric dimensions, or ruler in the mid-plane of the shock tube where the incident laser beam will illuminate an interface. These images are also used to convert image lengths from pixels to metric units. After experimental images are obtained, several post processing procedures follow.

Qualitative pre-processing adjusts the image intensity and removes background noise. A custom image processing script is used to determine the physical size of an interface during key points in time, catalogs and plots the data. The script works by first reading in an image and threshold filtering it to remove any background noise. A few image statistics such as the mean, median, maximum, and minimum intensity of the images are determined. The image is then searched pixel by pixel along its x and y axis for areas that exceed a set threshold intensity. This threshold is usually determined to be some percentage of the mean, median, or maximum intensity of the image.

The shock tube environment is dark (imaging mounts/ports covered with opaque cloths, dark room imaging) so the only light source received by the cameras comes from either the Mie scattering or fluorescence of the interface. This means the spots at which the threshold is exceeded will correspond to the edges of the interface flow field. The distance between x and y direction edges are calculated and taken to be the lengths the interface. These lengths can then be converted from pixels to metric units by using a conversion factor determined from the calibration image. The midpoint between bounds can also be found, which can be used to determine how symmetric the interface was.



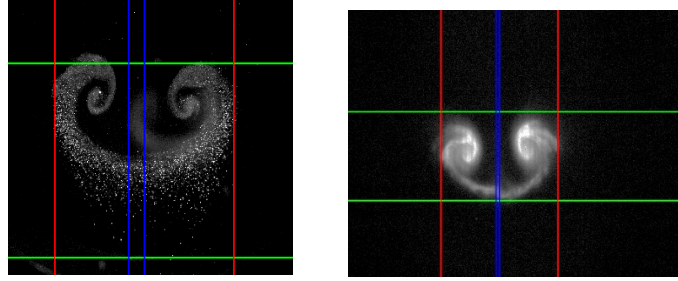


Figure 4.2 Plot of column averaged intensity values from shocked multiphase cylinder image with line demarking 20% intensity threshold (top), calculated interface bounds of particle (bottom left) and gas (bottom right) fields

An additional custom script resizes and maps images taken from the two cameras. In this way, an image of a particle field taken with the 4 MP camera can be resized and mapped such that it aligns with a corresponding gas field image taken with the 29 MP camera. Overlaying the images then shows the positions of both the gas and particle phase within a multiphase system at a particular instant in time.

Time separated image pairs were taken to obtain velocity measurements of both the particle and gas phase. For PIV, Insight 4G's proprietary PIV analysis and processing software was used in conjunction with custom post processing scripts to generate velocity fields from the shock accelerated liquid particles present in the interface. For comparison, this data was also analyzed using PIVlab⁷⁵⁻⁷⁷. PIVlab was also used to construct vector plots, as well as plots of velocity magnitude and vorticity tracked by the particles. For the gas phase, the Advection Corrected Correlation Image Velocimetry (ACCIV) technique along with custom post processing scripts were used to process time separated PLIF images into velocity data.

5 Results

5.1 Dynamic Imaging of Air-Water droplet Multiphase Cylinder

Three cases of a shock accelerated multiphase cylinder were considered. The initial perturbation was an approximately 12.5 mm diameter cylinder flowed continuously through the interface creation section of the shock tube in the direction of gravity. For case 1, the interface was comprised of the small 1.7 μm water particles and had an effective Atwood number of $.07 \pm .002$. Case 2 consisted of the same small diameter particles but possessed a much lower effective Atwood number of $.0140 \pm .003$. The third case was comprised of the 10.7 μm particles and processed an effective Atwood number of $.0140 \pm .0007$. From this point on: case 1 will refer to the high effective Atwood number, small particle diameter case; case 2 will refer to the low effective Atwood number small particle diameter case; and case 3 will refer to the low effective Atwood number, large particle diameter case.

Each case was accelerated by a planar $M=1.66$ shock wave traveling at ~ 570 m/s. (wave speed calculated from DPT data). The time at which the shock strikes the initial interface is taken to be $t=0$. After this point in time, the interface is accelerated to ~ 300 m/s and travels down the length of the test section for ~ 4300 μs . The post shock temperature is predicted by the shock tube relations to be ~ 418 K. Particle temperature are harder to predict, but a particle temperature of ~ 340 K has been estimated by previous simulation work done by lab members. Reshock occurs (reflected wave from end wall traverses upstream and intersects developing interface), re-accelerating the interface after 4300 μs . The interfaces velocity is effectively brought to 0 m/s at this time, but the interface continues to develop and evaporate rapidly. This is due to the high temperature

associated with reshock which is predicted from the shock tube relations to be ~ 564 K. A depiction of the interface transiting a portion of the test section after the initial acceleration is shown below.

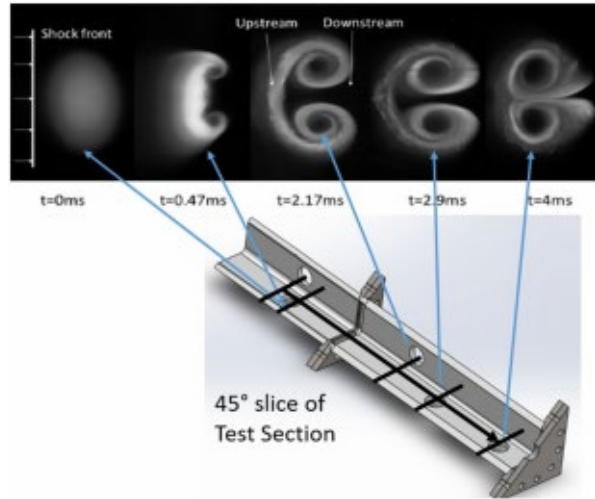


Figure 5.1 45° degree slice section view of shock tube test section with imaging locations and example images from those ports displayed

Images were taken at times corresponding to early, middle and late time development after an acceleration (incident and reshock) at which qualitative developmental changes could be captured by a camera placed at one of the viewports. The times were limited by spacing of the viewports. A developmental mosaic of the cases' development can be seen in Figure 5.2. The development can be described as an initial compression of the interface from the incident wave followed by the development of counter rotating vortices. The vortices begin to form at the edges of the interface as this is the point at which the gradient in momentum transfer will be greatest. As time progresses, the vortices dilate and extend into the surrounding air. This trend continues, slowing with time as energy is expended and moved to smaller length scales, until the interface is reshocked.

The re-acceleration of the interface introduces energy to a wider range of length scales present in the developed interface. This causes the distortion of large scale features, and the development of smaller scale structures. Reshock also raises the temperature of the surrounding gas, resulting in rapid evaporation of the particles within the interface. Droplets in small structures at the edges of the interface are quickly evaporated and mixed with the hot gas. As particles evaporate the interface structure and development becomes difficult, and eventually impossible, to discern in the particle Mie scattering image.

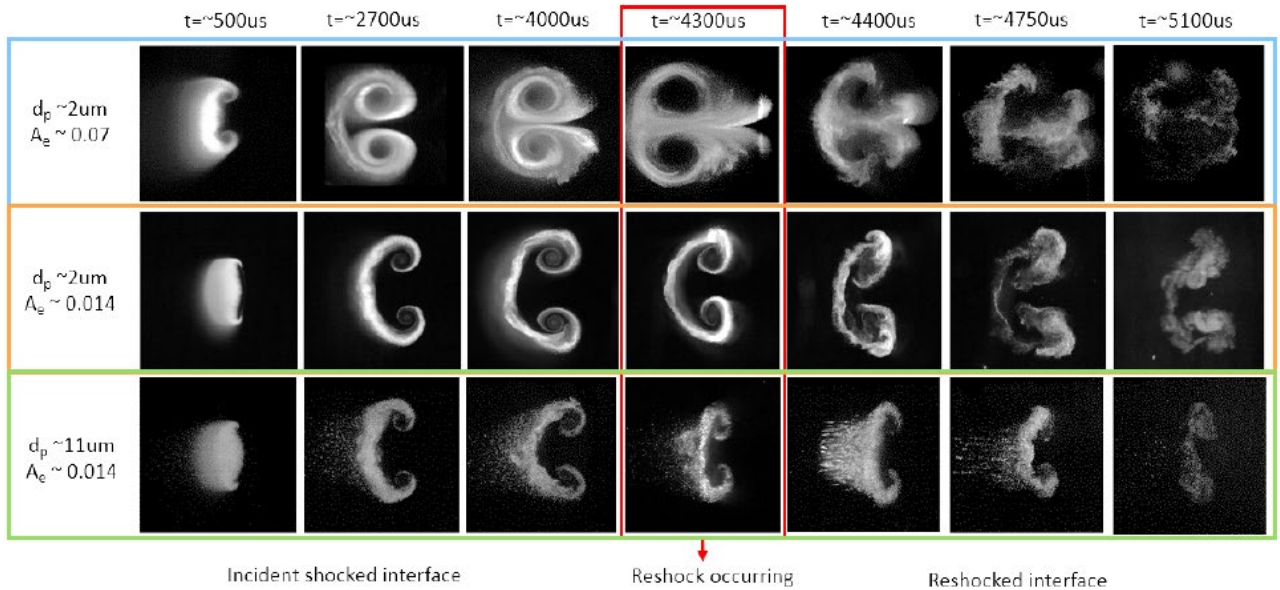


Figure 5.2 Mie scattering images of shocked multiphase cylinder taken to display cylindrical SDMI evolution at key times. All image frames were cropped to the same size, and the X and Y dimensions have been provided in an image for scale

5.2 Particle seeding affects

For case 1, a strong pair of counter rotating vortices form early on. At early and middle time development after the incident shock passage, the vortices dilate and begin to merge and a jet of particles extends out in front (downstream, right side in images) of the

interface. The jet is formed when particle clusters on the edges of the vortex pairs are unable to keep up with the rotational motion of the vortices and are flung out towards the opposite vortex. The clusters meet resistance from this vortex flow and are pushed in the downstream direction, in front of the interface

The intersection of the reshock wave with the ejected stream of particles can be seen in the frame depicting $t=4300\mu\text{s}$. The secondary acceleration causes a compression of the developing interface that is quickly overcome. The stem of ejected particles and vortex pair are distorted and secondary instabilities begin to form at the edges of the interface. These secondary instabilities move progressively inward into the large-scale structures of particle laden gas. The evaporation rate is dramatically increased after reshock and droplet concentration within the interface dissipated rapidly. Despite the high temperatures of reshock, many droplets located within large scale structures persist to late time as neighboring droplets shield one another through collective evaporative cooling of the surrounding gas.

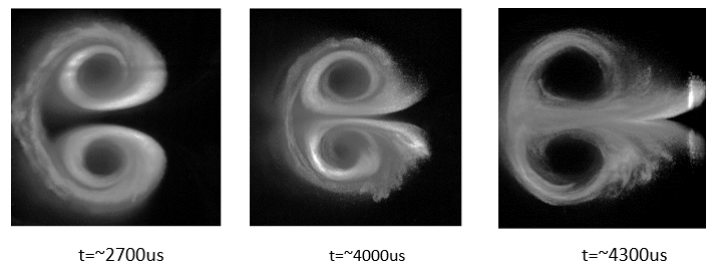


Figure 5.3 Fanning out of small particle that are ejected from the core of the vortices due to the intense rotational motion

Case 2 was brought to a lower effective Atwood number by mixing in a stream of non-particle seeded gas into the test flow, lowering the particle concentration. A pair of

well-defined, counter rotating vortices also develops early on in case 2. However, these vortices are connected by a thick band of test gas, and are much weaker when compared to case 1. As a result, the particles in case two are able to better follow the rotational motion of the vortex cores. This makes the vortices appear more organized and compact in comparison to case 1. As the vortex cores develop, the connecting band of test gas narrows as gas is drawn into the vortices. The edges of the vortices in case 2 remain sharp after incident shock as secondary instabilities do not form at their edges. In addition, no particle jet, as seen in case 1, forms. This is due to the lower particle seeding in this case, which has the effect of decreasing vortex strength.

After reshock, secondary instabilities do begin to form in case 2. Again, the reshock wave can be seen intersecting the developing interface at $t=4300 \mu\text{s}$. The reshock wave intersects the vortices first as there is no particle jet in this case. The interface is initially compressed after the secondary acceleration, although to a lesser extent than case 1. Small-scale vortices form at the edges of the band of connecting test gas, and larger vortices form around the vortex cores. The high temperature of reshock cause the rapid evaporation of droplets within the interface and as time progresses, imaging of the interface becomes difficult. However, structures remain more coherent compared to case 1, as small-scale turbulent like structures are slower to develop.

5.3 Particle relaxation time effects

Case 3 was brought to an effective Atwood number similar to case 2, but with larger ($10.7 \mu\text{m}$) diameter droplets. This allowed us to control for effective Atwood number while varying the droplet relaxation time. Case 3 exhibits further reduced

hydrodynamic growth with little to no growth after reshock. Before reshock, the two primary vortex cores form but are obviously weaker when compared to case 2. This can be seen as cores containing fewer rotations spiral from the circling particle field, and a lack of secondary features. The upstream particle layer is also thicker and spreads upstream (left in images) into a long tail of large, lagging particles. This tail forms early in the interface development and persists through reshock. Before reshock, these particles are large enough that they appear as well-defined circular outlines. Due to the sheer number of particles and a finite thickness of the laser sheet, some of the particles inevitably end up at the correct distance away from the focal plane to produce interferograms. These interferograms can be used in future works to estimate the size of particles trailing the bulk motion of the interface. For now, they at least qualitatively tell us that these particles are larger than the particles caught in the vortex cores.

Reshock causes the interface to compress in a similar manner to the other cases; however, the case 3 interface does not recover from the compression. There is also very little development of small-scale structures and the flow remain more organized and less turbulent in comparison. The high temperature gas brought about again increase the evaporation rate, but here the number of particles contained in the gas is much less and an evaporative cooling effect is not as present. This means that droplets evaporate rapidly making imaging impossible at later times when the interface may begin to attempt to recover from the reshock compression.

5.4 Aerodynamic breakup of large droplets

The reshock process makes droplet breakup easily observable in the tail region, as displayed in the figure below. This raises the question, what effect does droplet breakup have on the interface? Particle breakup models depend strongly on the weber number,

and weakly on other parameters such as the Ohnesorge number, or particle Reynolds number $Re_p = \frac{\rho_g u_g d_p}{\mu_g}$. For our cases, the Weber number varies greatly while the Ohnesorge and particle Reynolds number are small and don't have a significant effect on droplet behavior. The table below shows an estimate of these parameters over the average droplet sizes. The droplet temperature estimated from simulations is highly uniform among different droplet sizes and much lower than the surrounding gas. The Weber number divides the droplet break up into various regimes with different mechanisms and behaviors⁴⁰. The critical We was experimentally found to be ~ 12 , after which breakup is expected. The We is likely too small in the small droplet case for breakup to occur for either shock interaction.

For the $10.7 \mu\text{m}$ case, droplet breakup is likely to occur in both shock interactions. Breakup is difficult to observe in the first shock interaction as the droplets have a higher number density and it is difficult to resolve individual droplets until their differing lag times, τ_v , have spread them out somewhat. The We indicates that a bag breakup is likely, and based on previous work, it is possible to estimate the size and number of droplets.

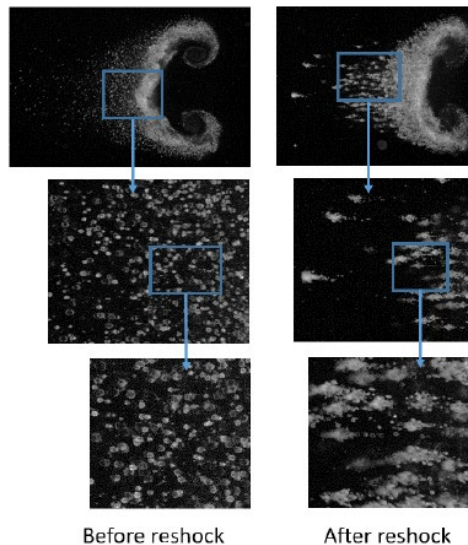


Figure 5.4 Aerodynamic breakup of large droplets present in tail of case 3 interface. Large particles are shattered into structured clusters of smaller particles.

Shock	d_p (μm)	We	Oh	Re_p
Incident	1.7	5.3	0.090	34
Incident	5.0	15.6	0.053	98
Incident	10.7	33.3	0.036	209
Reshock	1.7	11.3	0.040	55
Reshock	5.0	33	0.023	159
Reshock	10.7	70.6	0.016	341

Table 5.4 Particle breakup parameters

It should be noted that most works looking into droplet breakup are performed on much larger diameter (~ 1 mm) droplets and a few, if any, works have considered what additional effects might occur in the micron droplet diameter range. There will be a wide distribution of sizes resulting from this breakup and it is difficult to determine how neighboring droplet interactions and evaporation will modify the breakup process. It is likely then that some larger ($\sim 5\mu\text{m}$ estimated from images showing individual droplets in the tail) droplets will result and lag behind the interface forming the tail.

These large droplets undergo a secondary breakup process in reshock which can be observed in greater detail due to their lower number density. Before reshock, individual droplets can be identified in the tail. After reshock, these appear instead as large organized clusters of smaller droplets, with a distinct head-and-tail-like shape, where the tail is the portion extending to the right. The shape of the clusters may be the result of a bag-and-stamen breakup mode (consistent with We theory estimates). Here, small droplets sheared from the edges are accelerated rapidly by the post reshock

flow (velocity brought from ~300 m/s to essentially 0 m/s instantly) and remain in a tight cluster. Larger droplets formed from fragments of the core are slower to react to the reshock acceleration and continue to travel in the direction of incident shock. It is unknown how evaporation, neighboring droplets, and small diameters may affect the breakup process, but this is important to many applications of interest (e.g., fuel droplet evaporation) and warrants further analysis.

5.5 Mixing Width Plots

To facilitate quantitative analysis, a parameter termed mixing width was defined and plotted over the interface development at key times. The mixing width was defined as the distance the interface extended into surrounding gas in the direction of incident shock. This value was calculated using the post processing script for determining metric bounds of the interface within an image. The values were calculated for the bulk of the interface (counter rotating vortex pairs and band of connecting gas) as well as for auxiliary features (ejected particles and trailing tail of lagging particles). The results of the mixing width calculations can be seen below in Figure 5.5. The results agree with the qualitative results obtained from imaging.

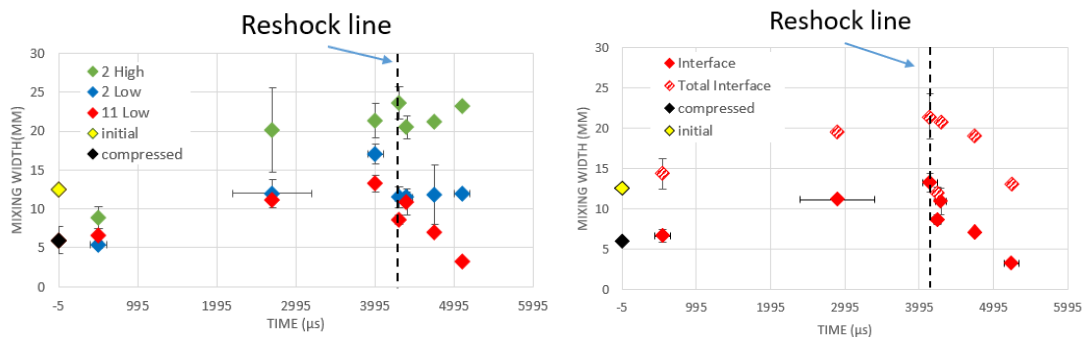


Figure 5.5 Mixing width plots for SDMI development. Mixing width plots of all 3 cases plotted (Left). Mixing width of case 3 with bulk interface and trailing tail considered (Right).

The first case (2 high) behaves very similar to an RM instability. The interface is initially compressed (decrease in mixing length) but then quickly rebounds and begins to grow rapidly. This continues until reshock occurs which sharply decreases the mixing width. After the secondary acceleration the interface rebounds and the mixing width steadily increases again and recovers its pre reshocked mixing length. The second case (2 low) the interface behaves similarly, but achieves lower overall values. The case also rebounds at a much slower rate after reshock and does not recover pre reshock mixing width. Comparing these two plotted cases again highlights just how strongly A_e affects the interface development. The higher particle seeding in case 1 creates a stronger momentum transfer gradient and initial vorticity deposition after initial acceleration. The vortex cores therefore dilate and stretch out into space more rapidly when compared to the low particle seeding case. This tendency persists even after reshock.

Comparing case three to case two depicts how particle size affects the interface growth. The momentum transfer process is similar between cases and the two mixing widths track closely to one another. However as time progresses, the continued advection of vorticity from the larger lagging particles in case three competes with the previously deposited vorticity; reducing the mixing width. This is depicted in the deviation of the case two and case three curves. After reshock, both cases show a sharp compression of the interface. Case 2 is able to rebound from this and attempts to recover its pre reshock mixing width. Case three however continues to rapidly compress after reshock. This highlights a unique multiphase effect. The larger particles of case three deplete the vorticity which seeks to dilate and stretch the interface as they lag behind the bulk of the flow. This interaction persists throughout the case three experiment even through reshock after many of the larger droplets have been broken up into clusters of smaller diameter particles.

The second plot shows the mixing width of the case three interface when the tail of trailing particles is taken into account in comparison to when just the bulk of the interface is considered. The estimation of the upstream edge of the tail was performed using a lower

threshold value for pixel intensity that corresponds to an interface edge location. This estimation was found to have a low sensitivity to threshold level selected. The development of the tail is similar to the bulk interface. The tail shows up almost immediately after incident shock acceleration and quickly equilibrates with the bulk flow until the secondary compression brought about by the reshock wave. After this, the tail length remains constant; the difference between total interface and interface with tail calculated mixing width is constant. It should be expected that the tail would shrink as the larger particles are slow to react in changes in acceleration and would want to move in the direction of the initial acceleration. Instead, the larger droplets breakup into small ones which equilibrate with the flow rapidly and hold the tail's upstream edge at a constant location.

5.6 Simultaneous PIV/PLIF Experiments

Simultaneous PIV/PLIF image pairs were taken to examine the gas and liquid phases of the shocked interface. The images were resized and overlaid for a qualitative representation of how the two phases interact through shock accelerations. Below is an example of a shock accelerated cylinder featuring particles of differing average sizes and seeding density. The top row shows a case representative of case 1 from the dynamic image mosaic ($d=1.7\mu m$, $A_e=.07$), while the bottom row shows a case of considerably lower seeding density utilizing the large ($d=10.7\mu m$, $A_e=.005$) particles. It should be noted that the seeding of acetone vapor (heavier than nitrogen or air) inevitably creates a gas Atwood number between the multiphase cylinder and surrounding medium; driving an RMI. This coupling of instabilities can actually be a desired effect, as it allows for an analysis of how the two instabilities interact. However, it is possible to remove this gas Atwood number and isolate purely SDMI behavior. This can be done by blending the test gas with a low density gas (e.g. helium) until the density of the test gas matches the

surrounding density. The images in figure 5.6 were taken without nulling the gas density difference, and feature interfaces with a gas Atwood number of approximately .05.

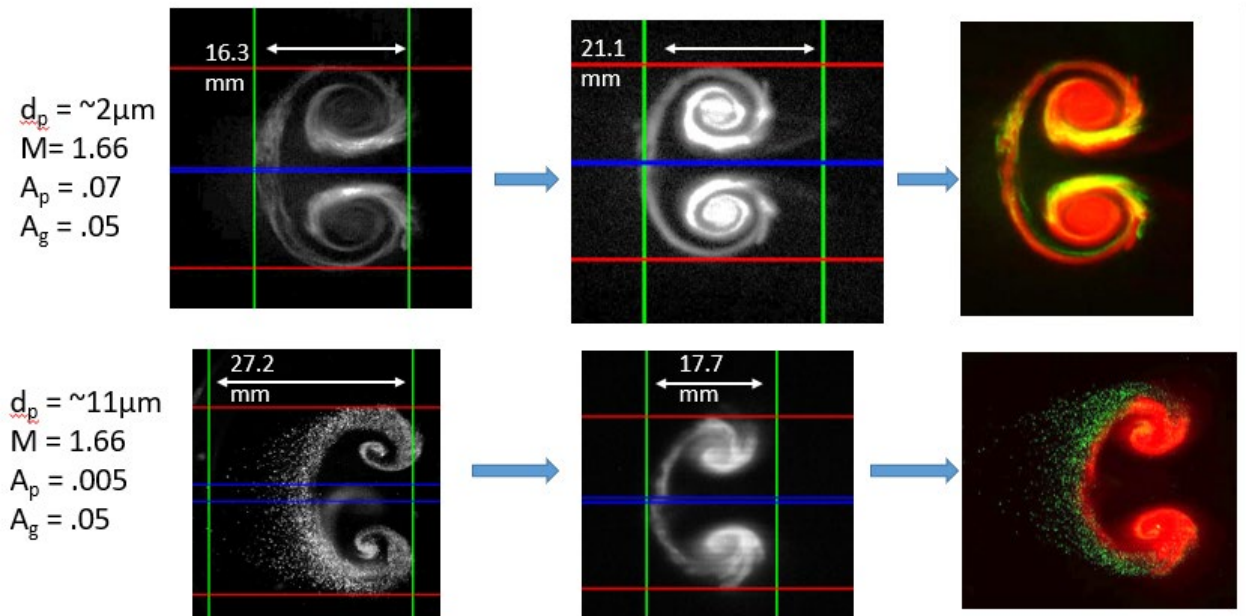


Figure 5.6 Simultaneous PIV/PLIF images of shock accelerated multiphase cylinder. Both images taken at ~ 4 ms after initial shock. First column: PIV image with metric bounds. Second column: PLIF images with metric bounds. Third column: Image overlays

From the images, it can be seen that while the particle and gas phase develop similarly, key differences can be identified. For the top row featuring the small fast reacting particles, both the gas and particles develop strong counter rotating vortices. The particles track the flow well and are the driving force behind the development. The unique gas effect elucidated here is the projecting jets that form upstream of vortex cores. This gas ejection from the vortex cores is a precursor to the downstream fan of particles that can be seen developing at late times after incident shock for this particular case.

For the second row, the average particle size is increased while the seeing density is lowered dramatically. This interface development is strongly driven by the gas Atwood number (RMI), however particles can still be seen affecting the flow development. The

vortex cores are diminished when compared to a pure RM instability of the same Atwood number. Additionally particles can be seen lagging behind the bulk of the interface (tracked perfectly by the gas), with the largest downstream particles lagging as far behind as ~ 9.5 mm.

5.7 PIV Analysis

PIV analysis was done using both Insight 4G and PIVlab⁷²⁻⁷⁴. For this particular experiment, an interface comprised of $10.7 \mu\text{m}$ acetone particles and nitrogen gas saturated with acetone vapor was shock accelerated. A Mach 1.66 shock was used to accelerate the flow field, and image pairs were taken at approximately $4100 \mu\text{s}$ after initial acceleration. A time separation of $1 \mu\text{s}$ between images was used. The seeding density of the interface produce an A_e of $\sim .022$. Large diameter acetone particle were chosen for this experiment in preparation for experiments that would involve reactive, volatile multiphase mixtures. Such experiments could mimic conditions relevant to high speed combustion applications, and would require both PIV and PLIF as a flow field diagnostic.

After image pairs were obtained, Insight was first used to generate velocity data. The analysis feature of the program allows for control of many parameters affecting accuracy of results. The input image pairs can be preprocessed with a Gaussian filter. This helps in the scenario where particle seeding is high, and particles can become too close together to distinguish individual particle. Gaussian filtering will make particles, which appear as uniformly bright point sources initially, appear as an airy discs with a clearly defined center. Regions of interest can be selected within an image so that analysis is focused in relevant areas and not wasted in regions of non-interest. The

method in which the image is gridded can also be controlled. The grid spacing (window size) can be set and the grid can be automatically set to satisfy a stability criterion (e.g. Nyquist grid based on an initial velocity estimate). Recursive methods can be applied which take an initial velocity field and use it as an input in a secondary analysis which would account for shearing and distortion of the field. The displacement of interrogation windows can also be controlled. Mean and median filtering of generated velocity fields can be performed to remove outliers as well as basic thresholding.

For this particular analysis, a Gaussian filter with a 5x5 pixel kernel size was applied to image pairs. A region of interest around the interface was selected and the image was discretized into a Nyquist grid. The grid was recursive and had a square spacing of 64x64 pixels for the first analysis pass, after which a secondary analysis pass at a spacing of 32x32 pixels was applied. A maximum window displacement of 50% of the window size was used. An FFT correlator was used for correlation calculations. After the vector field is generated the data is median filtered, first using a 7x7 point filter kernel then a 5x5 kernel. Data points which failed the filtering were replaced by the mean of the surrounding points. Vector thresholding was also applied, and vectors that did not come from a displacement with a correlation coefficient of at least 7 were removed and replaced with the local average.

Even after Insight pre and post processing, spurious vectors can (and often do) make it into the outputted velocity data. The velocity data can be exported from insight and imported into a custom filtering script. A filtering script was made which thresholds the velocity data by removing vectors that were 20% greater than the maximum predicted

flow velocity from 1D gas dynamics. Additional standard deviation filtering was performed recursively.

The 1D gas dynamics equations predict that gasses behind the initial shock should move at approximately the post shock velocity behind a Mach 1.66 shock (~ 300 m/s). This is assuming that the shock tube is perfectly sealed and that the accelerated flow is gaseous. Considering our shock tube is open to atmosphere, and our interface is seeded with particles that will pull momentum and energy from the surrounding gas, our predicted interface speed should be lower than this value. From tracking the interface throughout the shock tube, we have determined that the interface moves through the shock tube after initial acceleration at ~ 280 m/s.

Once the velocity data was verified to be within reason, vector plots and other quantitative measures could be obtained. A secondary PIV analysis was conducted using PIVlab. The results compared well to Insight analysis with a bulk interface velocity of ~ 276 m/s being calculated. From PIVlab, velocity vector plots were created along with pseudocolor plots of velocity magnitude and vorticity. The plots show the vector data with the bulk velocity (taken to be median velocity value in direction of incident shock transit) removed. Removing the overwhelming velocity induced by the post shock gas flow allows for more subtle dynamics (such as circulation around vortex cores) to be viewed. Results are shown below.

It can be seen that the two strong vortex cores are the dominant feature driving the flow throughout the interface after initial acceleration. The vortex cores have the effect of creating symmetric but reflecting regions of higher and lower velocity magnitude. This

has the effect of accelerating the flow around the vortex cores until a point is reached where the two cores interact and the competing vorticity decelerates the flow.

The strength of the vortex cores were found to be within reason when compared to similar work⁷⁸. Future work is required, but with the data obtained from PIV analysis statistical studies of interface dynamics and turbulence could be performed. As well as more detailed comparisons with numerical simulations.

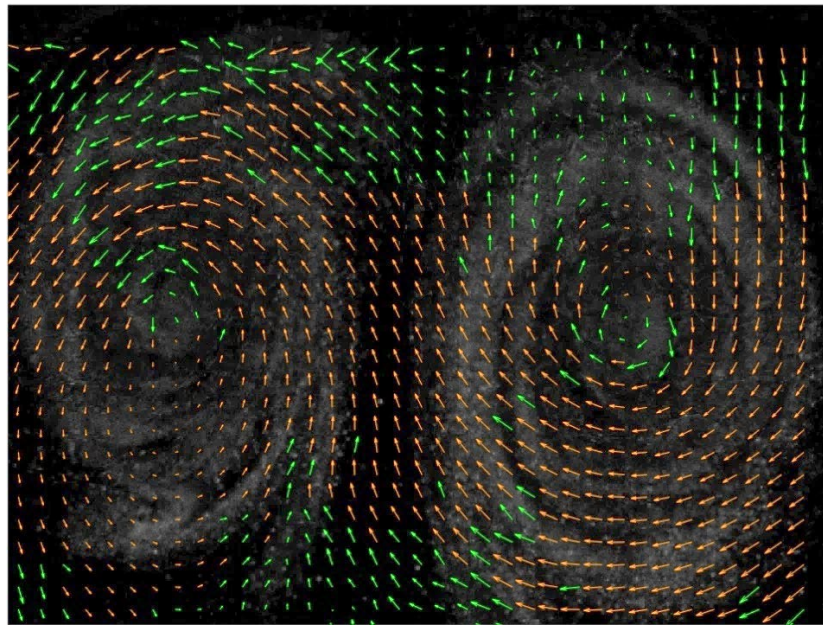


Figure 5.7 Velocity Vector Plot overlaid on corresponding image.

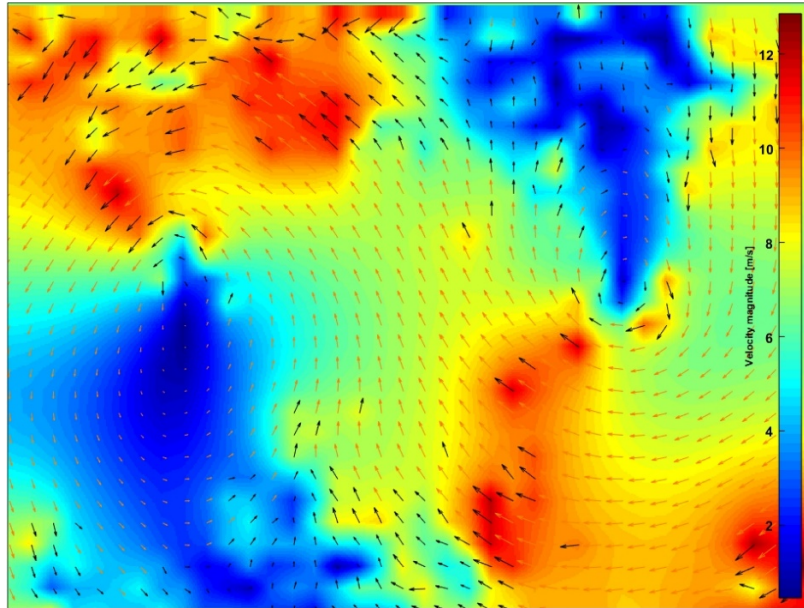


Figure 5.8 Pseudocolor plot of velocity magnitude overlaid with vector plot.

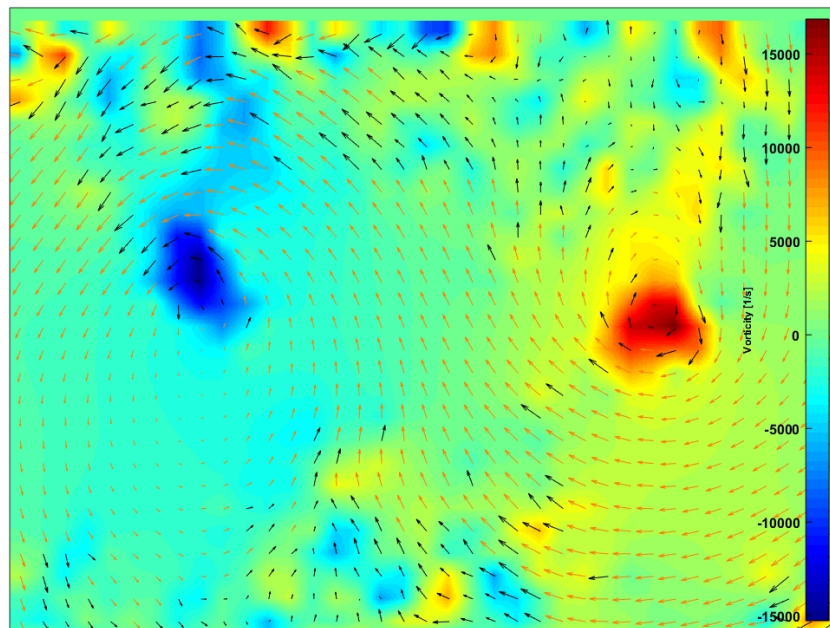


Figure 5.9 Pseudocolor plot of vorticity overlaid with vector plot. Major counter rotating vortex cores captured along with weaker deposited vorticity throughout the interface.

5.8 Gas Phase Velocity Measurements

Gas phase PLIF images were used to create velocity fields from shock accelerated interfaces. The image pairs were separated by a $1 \mu\text{s}$ time delay. The ACCIV method used works by first constructing a crude velocity field through image correlation. This crude velocity field is then used to numerically advect pixels forward and backward in time following the trajectory of the initial velocity. Uncertainties in the advection process will result in trajectories with inherent overshoots. A smooth curve is then interpolated between the two predicted trajectories creating a more realistic prediction of pixel trajectory and velocity. The process is iterated until the error (offset) between trajectories meets a convergence criteria. From the final velocity field construction, vector plots of gas velocity can be constructed.

This analysis again requires several pre and post processing procedures; many of which are similar to PIV processing procedures. Images must first be discretized into interrogation windows. ACCIV requires a recursive method so at least two analysis passes must be performed. For this work, an initial window size of 128×128 was first used to obtain the crude velocity field, and a 64×64 size window was used for remaining passes. A total of three analysis passes were used. The window displacement was set to 50% of the window size. An FFT correlator was used, and a minimum allowable correlation coefficient of .7 was set. The outputted data was processed in a similar manner to PIV data. A threshold of 20% greater than the maximum theoretical velocity was applied, and recursive standard deviation filtering was used. The local mean (calculated from 3 points forwards and backwards of the bad data point) was used to

replace data points that were filtered out. An example velocity histogram and vector field from this analysis are shown below.

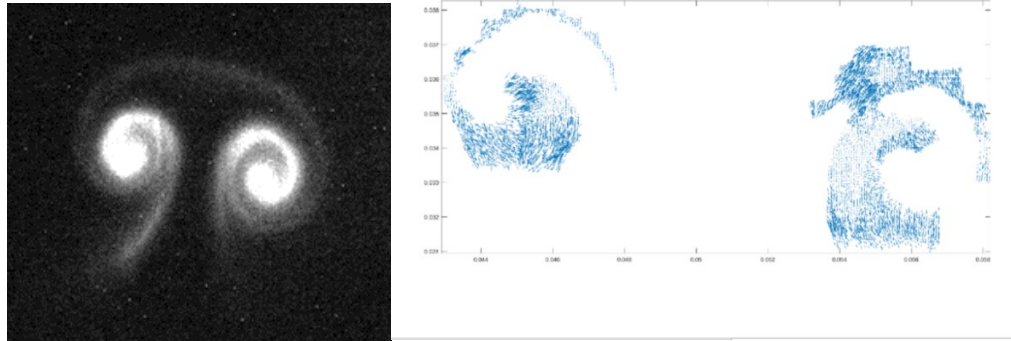


Figure 5.10 Example PLIF Image and ACCIV constructed velocity field calculated from Image pair

The technique is still being refined, but it has shown the ability to produce velocity data that can capture the bulk motion of the gas component of the interface. Improvements in the PLIF imaging technique could produce images with higher contrast. This would help the ACCIV program identify features of the interface to correlate between image frames, producing better velocity fields. This could be used in the future to obtain more advanced quantitative gas field properties (vorticity, circulation, turbulence statistics). Gas phase velocity fields could also be used in conjunction with particle velocity fields calculated from PIV to obtain full field velocity measures, as well as better quantify the effects of drag.

6 Conclusions

The SDMI is a unique multiphase flow instability that arises from an impulsive (shock) acceleration of a particle field. After acceleration, gradients in momentum transfer between the coupled particle and gas phases will result in the deposition of vorticity. This vorticity will act on the interface as it travels through the post shock flow, causing it to develop a strong pair of counter rotating vortex cores. These cores will stretch and dilate into the surrounding flow field, entraining and mixing particle-seeded and unseeded gasses. The development is similar to that of the RM instability, but differs considerably from RM development when multiphase effects are considered and enhanced.

This work presents preliminary qualitative and quantitative analysis of these multiphase effects. Particle seeding density has the effect of creating a stronger instability when it is higher as stronger momentum transfer gradients are present. Larger particles have the effect of lagging behind the bulk of the flow field and diminish the initially deposited vorticity. Both the RM and SDMI can coexist in the same environment and effects from both instabilities can be isolated and identified. A secondary acceleration (reshock) of the interface brings about a major change in flow field development and multiphase effects. This includes a rapid evaporation of small particles, formation of small-scale turbulent-like structures, and the aerodynamic breakup of larger particles into small clusters.

Non-intrusive flow visualization techniques such as PIV/PLIF and ACCIV were used to quantify multiphase effects. Interface dimensions throughout incident and reshock development were found and plotted. Simultaneous PIV/PLIF image overlays were created to show the relative positions and dynamics of the two phases at an instant. Plots of velocity vectors, velocity magnitude, and vorticity were also constructed to quantify vortex strength and flow movement within the interface.

Additional work is required and will be conducted to provide a more thorough investigation of shock driven multiphase hydrodynamics. This work will include statistical analysis of interface parameters, quantization of particle evaporation, comparisons to numerical simulations and theory, as well as extending the analysis to reacting flows and more complex systems.

References

- [1] McFarland, Jacob A., and Mark Hagenmaier. "Computational Study of Shock Driven Multiphase Mixing in Scramjet Conditions." *23rd AIAA Computational Fluid Dynamics Conference*. 2017.
- [2] Yang, Joseph, Toshi Kubota, and Edward E. Zukoski. "Applications of shock-induced mixing to supersonic combustion." *AIAA journal* 31.5 (1993): 854-862.
- [3] Nekkanti, Kishore. "Analysis Of Thrust Development In A Pulse Detonaton Engine." (2010).
- [4] Endo, Takuma, et al. "Reduction of air flow rate for pulse-detonation-turbine-engine operation by water-droplet injection." *Journal of Thermal Science and Technology* 11.2 (2016): JTST0022-JTST0022.
- [5] Kailasanath, K. "Liquid-fueled detonations in tubes." *Journal of Propulsion and Power* 22.6 (2006): 1261-1268.
- [6] Kasahara, Jiro, and Sergey Frolov. "Present status of pulse and rotating detonation engine research." *25th International Colloquium on the Dynamics of Explosions and Reactive Systems, paper*. Vol. 304. 2015.
- [7] Lu, Frank K., and Eric M. Braun. "Rotating detonation wave propulsion: experimental challenges, modeling, and engine concepts." *Journal of Propulsion and Power* 30.5 (2014): 1125-1142.
- [8] Schwer, Douglas, and Kailas Kailasanath. "Numerical investigation of the physics of rotating-detonation-engines." *Proceedings of the Combustion Institute* 33.2 (2011): 2195-2202.

- [9] Gardzilewicz, Andrzej, and Michal Kolovratnik. "Numerical and experimental investigations of steam condensation in LP part of a large power turbine." *Journal of Fluids Engineering* 131.4 (2009): 041301.
- [10] Colarossi, Michael, et al. "Multidimensional modeling of condensing two-phase ejector flow." *international journal of refrigeration* 35.2 (2012): 290-299.
- [11] Bianchi, Simone, and Raffaella Schneider. "Dust formation and survival in supernova ejecta." *Monthly Notices of the Royal Astronomical Society* 378.3 (2007): 973-982.
- [12] Woitke, Peter. "2D models for dust-driven AGB star winds." *Astronomy & Astrophysics* 452.2 (2006): 537-549.
- [13] Fagents, Sarah A., Tracy KP Gregg, and Rosaly MC Lopes, eds. *Modeling volcanic processes: the physics and mathematics of volcanism*. Cambridge University Press, 2013.
- [14] Richtmyer, Robert D. "Taylor instability in shock acceleration of compressible fluids." *Communications on Pure and Applied Mathematics* 13.2 (1960): 297-319.
- [15] Taylor, Geoffrey Ingram. "The instability of liquid surfaces when accelerated in a direction perpendicular to their planes. I." *Proceedings of the Royal Society of London. Series A. Mathematical and Physical Sciences* 201.1065 (1950): 192-196.
- [16] Meshkov, E. E. "Instability of the interface of two gases accelerated by a shock wave." *Fluid Dynamics* 4.5 (1969): 101-104.
- [17] McFarland, Jacob A., et al. "Computational study of the shock driven instability of a multiphase particle-gas system." *Physics of Fluids* 28.2 (2016): 024105.
- [18] Dahal, Jeevan, and Jacob A. McFarland. "A numerical method for shock driven multiphase flow with evaporating particles." *Journal of Computational Physics* 344 (2017): 210-233.
- [19] Benuzzi-Mounaix A, Koenig M, Ravasio A, Vinci T, Ozaki N, Le Gloahec MR, Loupias B, Huser G, Henry E, Bouquet S et al (2006) Laser-driven shock waves for the study of extreme matter states. *Plasma Phys Controll Fusion* 48(12B):B347

- [20] Robey HF, Kane J, Remington B, Drake R, Hurricane O, Louis H, Wallace R, Knauer J, Keiter P, Arnett D et al (2001) An experimental testbed for the study of hydrodynamic issues in supernovae. *Phys Plasmas* 8(5):2446–2453
- [21] Courtney E, Courtney A, Courtney M (2014) Shock tube design for high intensity blast waves for laboratory testing of armor and combat materiel. *Def Technol* 10(2):245–250
- [22] Ranjan D, Oakley J, Bonazza R (2011) Shock–bubble interactions. *Annu Rev Fluid Mech* 43(1):117–140.
- [23] McFarland J, Reilly D, Creel S, McDonald C, Finn T, Ranjan D (2014) Experimental investigation of the inclined interface Richtmyer–Meshkov instability before and after reshock. *Exp Fluids* 55(1):1–14.
- [24] Wilson BM, Mejia-Alvarez R, Prestridge KP (2016) Single-interface Richtmyer–Meshkov turbulent mixing at the los alamos vertical shock tube. *J Fluids Eng* 138(7):070901
- [25] Dahal, Jeevan, and Jacob A. McFarland. "A numerical method for shock driven multiphase flow with evaporating particles." *Journal of Computational Physics* 344 (2017): 210-233.
- [26] Mohaghar, Mohammad, et al. "Evaluation of turbulent mixing transition in a shock-driven variable-density flow." *Journal of Fluid Mechanics* 831 (2017): 779-825.
- [27] McFarland, Jacob A., et al. "Modal interactions between a large-wavelength inclined interface and small-wavelength multimode perturbations in a Richtmyer-Meshkov instability." *Physical Review E* 92.1 (2015): 013023.
- [28] Schilling, Oleg, Marco Latini, and Wai Sun Don. "Physics of reshock and mixing in single-mode Richtmyer-Meshkov instability." *Physical Review E* 76.2 (2007): 026319.
- [29] Ranjan D, Oakley J, Bonazza R (2011) Shock–bubble interactions. *Annu Rev Fluid Mech* 43(1):117–140.
- [30] Luo X, Guan B, Si T, Zhai Z, Wang X (2016) Richtmyer–Meshkov instability of a three-dimensional SF6-air interface with a minimum-surface feature. *Phys Rev E* 93(1):013101

- [31] Motl B, Oakley J, Ranjan D, Weber C, Anderson M, Bonazza R (2009) Experimental validation of a Richtmyer–Meshkov scaling law over large density ratio and shock strength ranges. *Phys Fluids* 21(126):102
- [32] Collins BD, Jacobs JW (2002) PLIF flow visualization and measurements of the Richtmyer–Meshkov instability of an air/SF₆ interface. *J Fluid Mech* 464:113–136.
- [33] Mohaghar M, Carter J, Musci B, Reilly D, McFarland JA, Ranjan D (2017) Evaluation of turbulent mixing transition in a shock-driven variable-density flow. *J Fluid Mech* 831:779–825.
- [34] McFarland J, Reilly D, Creel S, McDonald C, Finn T, Ranjan D (2014) Experimental investigation of the inclined interface Richtmyer–Meshkov instability before and after reshock. *Exp Fluids* 55(1):1–14.
- [35] Weber C, Haehn N, Oakley J, Rothamer D, Bonazza R (2012) Turbulent mixing measurements in the Richtmyer–Meshkov instability. *Phys Fluids* 24(7):074105
- [36] Wilson BM, Mejia-Alvarez R, Prestridge KP (2016) Single-interface Richtmyer–Meshkov turbulent mixing at the los alamos vertical shock tube. *J Fluids Eng* 138(7):070901
- [37] Haas JF, Sturtevant B (1987) Interaction of weak shock waves with cylindrical and spherical gas inhomogeneities. *J Fluid Mech* 181:41–76
- [38] Jacobs JW (1992) Shock-induced mixing of a light-gas cylinder. *J Fluid Mech* 234:629–649.
- [39] Tomkins C, Prestridge K, Rightley P, Marr-Lyon M, Vorobieff P, Benjamin R (2003) A quantitative study of the interaction of two Richtmyer–Meshkov-unstable gas cylinders. *Phys Fluids* 15(4):986–1004
- [40] Vorobieff P, Anderson M, Conroy J, White R, Truman CR, Kumar S (2011) Vortex formation in a shock-accelerated gas induced by particle seeding. *Phys Rev Lett* 106(18):184503
- [41] Marble, Frank E. "Dynamics of dusty gases." *Annual Review of Fluid Mechanics* 2.1 (1970): 397-446.
- [42] Hsiang, L-P., and G. M. Faeth. "Drop deformation and breakup due to shock wave and steady disturbances." *International Journal of Multiphase Flow* 21.4 (1995): 545-560.

- [43] Jalaal, M., and K. Mehravaran. "Fragmentation of falling liquid droplets in bag breakup mode." *International Journal of Multiphase Flow* 47 (2012): 115-132.
- [44] Craig L, Moharreri A, Schanot A, Rogers DC, Anderson B, Dhaniyala S (2013) Characterizations of cloud droplet shatter artifacts in two airborne aerosol inlets. *Aerosol Sci Technol* 47(6):662–671
- [45] Guildenbecher DR, Lopez-Rivera C, Sojka PE (2009) Secondary atomization. *Exp Fluids* 46(3):371–402.
- [46] Black, Wolfgang J., Nicholas A. Denissen, and Jacob A. McFarland. "Evaporation Effects in Shock-Driven Multiphase Instabilities." *Journal of Fluids Engineering* 139.7 (2017): 071204.
- [47] Paudel, Manoj, Jeevan Dahal, and Jacob McFarland. "Particle evaporation and hydrodynamics in a shock driven multiphase instability." *International Journal of Multiphase Flow* 101 (2018): 137-151.
- [48] Parmar M, Haselbacher A, Balachandar S (2009) Prediction and modeling of shock-particle interaction. In: 47th AIAA aerospace sciences meeting including the new horizons forum and aerospace exposition, p 1124
- [49] Parmar M, Haselbacher A, Balachandar S (2010) Improved drag correlation for spheres and application to shock-tube experiments. *AIAA J* 48(6):1273–1276.
- [50] Anderson M, Vorobieff P, Truman CR, Corbin C, Kuehner G, Wayne P, Conroy J, White R, Kumar S (2015) An experimental and numerical study of shock interaction with a gas column seeded with droplets. *Shock Waves* 25(2):107–125.
- [51] Schulz JC, Gottiparthi KC, Menon S (2013) Richtmyer–Meshkov instability in dilute gas-particle mixtures with re-shock. *Phys Fluids* 25(11):114105.

- [52] Davis SL, Dittmann TB, Jacobs GB, Don WS (2013) Dispersion of a cloud of particles by a moving shock: effects of the shape, angle of rotation, and aspect ratio. *J Appl Mech Tech Phys* 54(6):900–912.
- [53] McFarland JA, Black WJ, Dahal J, Morgan BE (2016) Computational study of the shock driven instability of a multiphase particle-gas system. *Phys Fluids* 28(2):024–105
- [54] Annamalai S, Rollin B, Ouellet F, Neal C, Jackson TL, Balachandar S (2016) Effects of initial perturbations in the early moments of an explosive dispersal of particles. *J Fluids Eng* 138(7):070903
- [55] Puthenveetil, Baburaj A., and E. J. Hopfinger. "Evolution and breaking of parametrically forced capillary waves in a circular cylinder." *Journal of Fluid Mechanics* 633 (2009): 355-379
- [56] Lang, Robert J. "Ultrasonic atomization of liquids." *The journal of the acoustical society of America* 34.1 (1962): 6-8.
- [57] Donnelly, Thomas D., et al. "Using ultrasonic atomization to produce an aerosol of micron-scale particles." *Review of scientific instruments* 76.11 (2005): 113301.
- [58] Berglund, Richard N., and Benjamin YH Liu. "Generation of monodisperse aerosol standards." *Environmental Science & Technology* 7.2 (1973): 147-153.
- [59] Lefebvre A, McDonell V (2017) *Atomization and sprays*. CRC Press, Boca Raton
- [60] Goodridge, Christopher L., W. Tao Shi, and Daniel P. Lathrop. "Threshold dynamics of singular gravity-capillary waves." *Physical review letters* 76.11 (1996): 1824.
- [61] Chen, Co Yo. "Filtration of aerosols by fibrous media." *Chemical Reviews* 55.3 (1955): 595-623.
- [62] Mie, Gustav. "Beiträge zur Optik trüber Medien, speziell kolloidaler Metallösungen." *Annalen der physik* 330.3 (1908): 377-445.

- [63] Hulst, Hendrik Christoffel, and Hendrik C. van de Hulst. *Light scattering by small particles*. Courier Corporation, 1957.
- [64] König, G., K. Anders, and A. Frohn. "A new light-scattering technique to measure the diameter of periodically generated moving droplets." *Journal of aerosol science* 17.2 (1986): 157-167
- [65] Tran, T., Y. Kochar, and J. Seitzman. "Measurements of liquid acetone fluorescence and phosphorescence for two-phase fuel imaging." AIAA Paper 2005-0827, 43rd AIAA Aerospace Sciences Meeting and Exhibit. 2005.
- [66] Ritchie, B., and J. Seitzman. "Quantitative acetone PLIF in two-phase flows." 39th Aerospace Sciences Meeting and Exhibit. 2001.
- [67] Löffler, Micha, Frank Beyrau, and Alfred Leipertz. "Acetone laser-induced fluorescence behavior for the simultaneous quantification of temperature and residual gas distribution in fired spark-ignition engines." *Applied optics* 49.1 (2010): 37-49.
- [68] Pust, Oliver. "Piv: Direct cross-correlation compared with fft-based cross-correlation." Proceedings of the 10th International Symposium on Applications of Laser Techniques to Fluid Mechanics, Lisbon, Portugal. Vol. 27. 2000
- [69] Martinez AA, Orlicz GC, Prestridge KP (2015) A new experiment to measure shocked particle drag using multi-pulse particle image velocimetry and particle tracking. *Exp Fluids* 56(1):1854.
- [70] Aure, Roger, and Jeffrey W. Jacobs. "Particle image velocimetry study of the shock-induced single mode Richtmyer–Meshkov instability." *Shock Waves* 18.3 (2008): 161-167.

- [71] Prestridge, K., et al. "Validation of an instability growth model using particle image velocimetry measurements." *Physical review letters* 84.19 (2000): 4353.
- [72] Mohaghar, Mohammad, et al. "Evaluation of turbulent mixing transition in a shock-driven variable-density flow." *Journal of Fluid Mechanics* 831 (2017): 779-825.
- [73] Asay-Davis, Xylar S., et al. "Jupiter's shrinking Great Red Spot and steady Oval BA: Velocity measurements with the 'Advection Corrected Correlation Image Velocimetry' automated cloud-tracking method." *Icarus* 203.1 (2009): 164-188.
- [74] Reese, Daniel, et al. "Simultaneous concentration and velocity field measurements in a shock-accelerated mixing layer." *Experiments in fluids* 55.10 (2014): 1823.
- [75] Thielicke, W. and Stamhuis, E.J. (2014): PIVlab – Towards User-friendly, Affordable and Accurate Digital Particle Image Velocimetry in MATLAB. *Journal of Open Research Software* 2(1):e30, DOI: <http://dx.doi.org/10.5334/jors.bl>
- [76] Thielicke, W. and Stamhuis, E. J. (2014): PIVlab - Time-Resolved Digital Particle Image Velocimetry Tool for MATLAB (version: X.XX modify this).
<http://dx.doi.org/10.6084/m9.figshare.1092508>
- [77] Thielicke, W. (2014): The Flapping Flight of Birds - Analysis and Application. Phd thesis, Rijksuniversiteit Groningen. <http://irs.ub.rug.nl/ppn/382783069>
- [78] Goodenough, Cherie, et al. "Planar velocity and scalar concentration measurements in shock-accelerated unstable fluid interfaces." 26th International Congress on High-Speed Photography and Photonics. Vol. 5580. International Society for Optics and Photonics, 2005.